# Intrinsic structural instabilities of domain walls driven by gradient coupling: Meandering antiferrodistortive-ferroelectric domain walls in $BiFeO_3$

Eugene A. Eliseev,[1] Anna N. Morozovska,[2] Christopher T. Nelson,[3] and Sergei V. Kalinin[3,*]

[1] *Institute for Problems of Materials Science, National Academy of Sciences of Ukraine, Krjijanovskogo 3, 03142 Kyiv, Ukraine*
[2] *Institute of Physics, National Academy of Sciences of Ukraine, 46, Prospekt Nauky, 03028 Kyiv, Ukraine*
*and Bogolyubov Institute for Theoretical Physics, National Academy of Sciences of Ukraine, 14-b Metrolohichna street 03680 Kyiv, Ukraine*
[3] *The Center for Nanophase Materials Sciences, Oak Ridge National Laboratory, Oak Ridge, Tennessee 37831, USA*

(Received 16 October 2018; revised manuscript received 31 December 2018; published 25 January 2019)

Using the Landau-Ginzburg-Devonshire approach, we predict the intrinsic instability of the ferroelectric-ferroelastic domain walls in the multiferroic $BiFeO_3$ emerging from the interplay between the gradient terms of the antiferrodistortive and ferroelectric order parameters at the walls. These instabilities are the interface analog of the structural instabilities in the vicinity of phase coexistence in the bulk, and so they do not stem from incomplete polarization screening in thin films or its spatial confinement, electrostrictive or flexoelectric coupling. The effect of $BiFeO_3$ material parameters on the 71°, 109°, and 180° walls is explored, and it is shown that the meandering instability appears at 109° and 180° walls for small gradient energies, and the walls become straight and broaden for higher gradients. In contrast to the 180° and 109° domain walls, uncharged 71° walls are always straight, and their width increases with increasing the tilt gradient coefficient. The wall instability and associated intrinsic meandering provide insight into the behavior of morphotropic and relaxor materials, wall pinning, and mechanisms of interactions between order parameter fields and local microstructure.

DOI: 10.1103/PhysRevB.99.014112

## I. INTRODUCTION

Multiferroics, defined as materials with more than one ferroic long-range order [1–3], are ideal systems for fundamental studies of couplings among the order parameters of different nature, e.g., ferroelectric (FE) polarization, structural antiferrodistortion (AFD), ferromagnetic (FM), and antiferromagnetic (AFM) order parameters [4–11]. The AFD, FE, FM, and AFM degrees of freedom in multiferroics are interlinked via different types of biquadratic couplings leading to versatile phase diagrams and complex domain structures [4–11]. In many cases, the interaction of the domain structures with underpinning frozen disorder gives rise to highly mobile structures and materials with giant functional responses.

The biquadratic couplings between AFD and other long-range orders are universal for all multiferroics with rotational antiferrodistortive symmetry [12]. The most common is the Houchmandazeh-Laizerowicz-Salje coupling, which is the biquadratic coupling between the AFD order parameter and FE polarization [13,14]. AFD-FE coupling can significantly influence the structure and local properties of domain walls in AFD multiferroics [15,16]. Similarly, the biquadratic magnetoelectric coupling, which is the coupling between polarization and magnetization [4,5], can influence phase diagrams, domain wall structure, and morphology [17]. The bilinear flexoelectric coupling [18], that coupled the strain gradient with polarization and vice versa, can induce incommensurate spatially modulated phases in ferroics including antiferroelectric (AFE) and AFD ones [19–22]. The flexoantiferrodistortive coupling, inherent to all AFD systems, can lead to the formation of incommensurate, spatially modulated AFD and AFE phases in multiferroics [23], which are indeed observed in, e.g., $Bi_ySm_{1-y}FeO_3$ [19] and $EuTiO_3$ [24,25]. There are also a wide variety of spatially modulated domain structures observed experimentally at the morphotropic boundaries in (multi)ferroics [26–30].

The vectorial nature of the AFD order parameter can strongly influence the phase stability, domain structure, polar, dielectric, and magnetoelectric properties of (multi)ferroic thin films [31–33]. Sometimes phase diagrams of thin strained films are complicated by unusual low symmetry phases, which are absent in their bulk counterparts [34–37]. Vortices and vertices composed by the closure of domain walls have been observed experimentally in nanoscale multiferroics [38,39], especially in $BiFeO_3$ (BFO) [40,41]. Fractal domain structures have been observed in multiferroic thin films [42] and near the surface of ferroelectric relaxors close to relaxor-ferroelectric transition [43].

Unusual polar structures with domain walls of labyrinthine shape (shortly "labyrinthine domain structure") have been observed near the surface of relaxors with so-called "ergodic phases" [44–46]. The labyrinthine domain structure was calculated theoretically in thin films of incommensurate and bilayered ferroelectrics [47,48], being similar to those observed in ultrathin magnetic films [49]. Spherical nanoparticles of uniaxial ferroelectrics $CuInP_2S_6$ and $Sn_2P_2S_6$ covered by a layer of screening charge with finite screening length revealed the transformation from a regular stripe domain structure into a labyrinthine one when the polarization gradient energy decreases below the critical value [50,51]. The transformation can be identified as a gradient-driven morphological

---

[*] sergei2@ornl.gov

transition, and appeared unrelated with flexoelectric or electrostrictive, or any other bilinear or biquadratic coupling influence.

To the best of our knowledge the physical origin of the complex morphology of domain structures and modulated phases in nanoscale ferroics is the imbalance between domain wall surface energy and electrostatic or magnetic (or possibly elastic) energy contributions. Specifically, a ferroelectric nanoparticle tends to minimize its electrostatic energy by creation of the complex or/and irregular features of domain structure near the free surfaces, but the structure cannot be too fine scale due to the increasing energy of domain walls (see, e.g., discussion in Refs. [50,51]). A much more complex situation, corresponding to the balance of labyrinthine domain structure in the bulk and vortices at the surface, is expected in multiaxial ferroelectrics with polarization rotation allowed, such as $BaTiO_3$, $(Pb, Zr)TiO_3$, and BFO, and the fundamental question about the instability threshold of regular domain structure in nanoscale multiaxial multiferroics remains open.

The gap in the knowledge motivates this work that reveals a meandering zigzaglike instability of AFD-FE domain walls in thin BFO films. This unexpected result, obtained by finite element modeling (FEM), is explained within a Landau-Ginzburg-Devonshire (LGD) theory framework.

The original part of the paper is structured as follows. LGD free energy is given in Sec. II A. The problem statement including the film geometry, and brief form of the coupled Euler-Lagrange equations with boundary conditions, is described in Sec. II B. The impact of biquadratic coupling on the stability of homogeneous phases is analyzed in Sec. II C. Simulation details with special attention to the measures taken to establish the physical origin of the complex domain morphologies are described in Sec. III A. The appearance of low symmetry phases limited by 180° or 109° zigzaglike meandering AFD-FE domains and their changes with increasing of the gradient energy are presented in Secs. III B and III C, respectively. The gradient-driven broadening of AFD-FE 71° domain walls is discussed in Sec. III D. Section IV is a brief summary. Evident forms of the free energy, boundary conditions, and material parameters, as well as supplemental figures are given in the Supplemental Material [52].

## II. THEORETICAL FORMALISM

As a model system, we have chosen bismuth ferrite, BFO. Pristine and rare-earth doped BFO is the unique multiferroic [53,54] with a strong FE polarization, AFD oxygen octahedron rotation, and FM and AFM long-range orders coexisting up to room and elevated temperatures. Specifically bulk BFO exhibits AFD long-range order at temperatures below 1200 K; it is FE with a large spontaneous polarization below 1100 K and AFM below the Néel temperature $T_N \approx 650\,\mathrm{K}$ [55]. Notably the behavior of the AFD order parameter at the BFO domain walls determines their structure and energy [56]. Domain walls in BFO exhibit unusual electrophysical properties, such as conduction and magnetotransport enhancement [57–62]. Recently, a complete phase diagram of BFO including the AFM, FE, and AFD phases was calculated within LGD theory [63].

The pronounced multiferroic properties and unusual domain structure evolution maintain in BFO thin films and heterostructures [64–72]. In particular, atomic mapping of structural distortions in 109° domains revealed that the coexistence of rhombohedral and orthorhombic phases in ultrathin BFO films can be driven by interfacial oxygen octahedral coupling [73,74]. The role of the rotomagnetic coupling, which is the biquadratic coupling between the AFD and AFM (or FM) orders [75], has been studied in BFO fine grained ceramics [76].

### A. Landau-Ginzburg-Devonshire free energy

The thermodynamic LGD potential $G$ that describes AFD, FE, and AFM properties of BFO is

$$G = \int_V (\Delta G_{\mathrm{AFD}} + \Delta G_{\mathrm{FE}} + \Delta G_{\mathrm{AFM}} + \Delta G_{\mathrm{BQC}} + \Delta G_{\sigma})dv + \int_S (\Delta G_{\mathrm{AFD}} + \Delta G_{\mathrm{FE}})dS. \tag{1}$$

The AFD energy $\Delta G_{\mathrm{AFD}}$, corresponding to the $R3c$ phase, is a six-order expansion on the oxygen tilt $\Phi_i$ and its gradients,

$$\Delta G_{\mathrm{AFD}} = b_i(T)\Phi_i^2 + b_{ij}\Phi_i^2\Phi_j^2 + b_{ijk}\Phi_i^2\Phi_j^2\Phi_k^2 + v_{ijkl}\frac{\partial\Phi_i}{\partial x_k}\frac{\partial\Phi_j}{\partial x_l}. \tag{2}$$

Here $\Phi_i$ are components of the pseudovector determining the out-of-phase static rotations of the oxygen octahedral groups, and the Einstein summation convention is employed. In accordance with the classical LGD theory, we assume that the coefficients $b_i$ are temperature dependent in accordance with the Barrett law [77], $b_i = b_T T_{q\Phi}[\coth(T_{q\Phi}/T) - \coth(T_{q\Phi}/T_\Phi)]$, where $T_\Phi$ is the AFD transition temperature, and $T_{q\Phi}$ is a Barrett temperature [78].

FE energy $\Delta G_{\mathrm{FE}}$ is a six-order expansion on the polarization vector $P_i$ and its gradients,

$$\Delta G_{\mathrm{FE}} = a_i(T)P_i^2 + a_{ij}P_i^2P_j^2 + a_{ijk}P_i^2P_j^2P_k^2 + g_{ijkl}\frac{\partial P_i}{\partial x_k}\frac{\partial P_j}{\partial x_l} - P_iE_i - \frac{\varepsilon_0\varepsilon_b}{2}E_i^2. \tag{3}$$

The coefficients $a_k$ are temperature dependent, $a_k^{(P)} = \alpha_T[T_{qP}\coth(T_{qP}/T) - T_C]$, where $T_C$ is a Curie temperature, and $T_{qP}$ is the characteristic Barrett temperature related with some "vibrational modes" [77]. Other coefficients in Eqs. (3) are temperature independent. $E_i$ are the components of the internal electric field related with electrostatic potential $\varphi$ in a standard way, $E_i = -\partial\varphi/\partial x_i$. Universal dielectric constant is $\varepsilon_0$; $\varepsilon_b$ is the dielectric permittivity of the background [18,79].

AFM energy $\Delta G_{\mathrm{AFM}}$ is a fourth-order expansion in terms of the AFM order parameter vector $L_i$ and its gradient, as follows from the fact that this phase transition in BFO is second order [63]. The details of $\Delta G_{\mathrm{AFM}}$ are considered elsewhere [63].

The AFD-FE coupling energy $\Delta G_{\mathrm{BQC}}$ is the biquadratic function of $P_i$ and $\Phi_i$:

$$\Delta G_{\mathrm{BQC}} = \zeta_{ijkl}\Phi_i\Phi_jP_kP_l. \tag{4}$$

The temperature-independent coefficients $\zeta_{ijkl}$ are the components of the AFD-FE biquadratic coupling tensor.

The elastic, electrostriction, rotostriction, and flexoelectric energy are

$$\Delta G_\sigma = -\frac{1}{2}s_{ijkl}\sigma_{ij}\sigma_{kl} - Q_{ijkl}\sigma_{ij}P_kP_l - R_{ijkl}\sigma_{ij}\Phi_k\Phi_l - \frac{F_{ijkl}}{2}\left(\sigma_{ij}\frac{\partial P_k}{\partial x_l} - P_k\frac{\partial \sigma_{ij}}{\partial x_l}\right). \quad (5)$$

Here $s_{ijkl}$ are the components of the elastic compliances tensor, $Q_{ijkl}$ are the components of the electrostriction tensor, $R_{ijkl}$ are the components of the rotostriction tensor, and $F_{ijkl}$ are the components of the flexoelectric tensor.

The surface energy has the form

$$\int_S (\Delta G_{\mathrm{AFD}} + \Delta G_{\mathrm{FE}})dS = \int_S \left(\frac{b_i^{(S)}}{2}\Phi_i^2 + \frac{a_i^{(S)}}{2}P_i^2\right)dS. \quad (6)$$

Surface energy coefficients $b_i^{(S)}$ and $a_i^{(S)}$ have a different nature and control the broadening of ADF and FE domain walls at the surface, respectively.

### B. Problem statement

Let us consider a BFO film of thickness $h$ placed in a perfect electric contact with conducting bottom electrode that mechanically clamps the film. The top surface of the film is mechanically free and can be in ideal electric contact with the top electrode, or electrically open, or covered with the surface screening charge. The charge density $\sigma\ (\varphi)$, appearing due to surface states [80], or electrochemically active ions [81–84], depends on the electric potential $\varphi$ [see Fig. 1(a)]. Figures 1(b)–1(d) show three types of nominally uncharged 180°, 109°, and 71° domain walls in BFO.

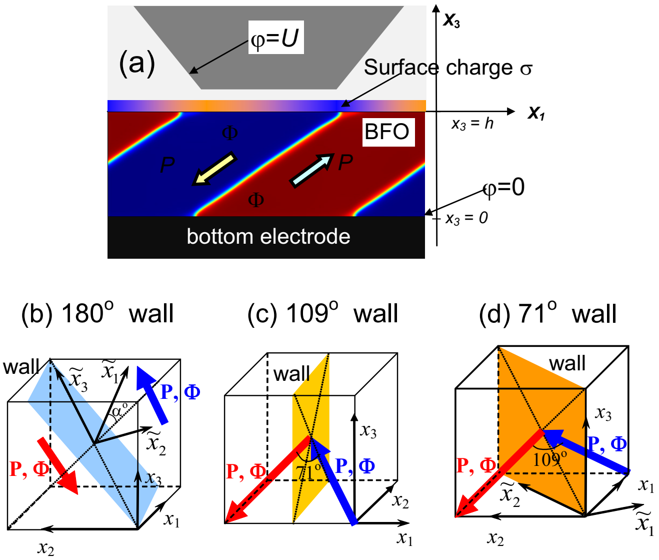

FIG. 1. (a) Considered system, consisting of electrically conducting bottom electrode, BFO film of thickness $h$ with a domain structure, surface screening charge with density $\sigma\ (\varphi)$, and ambient media (from bottom to the top). Three types of nominally uncharged 180° (b), 109° (c), and 71° (d) domain walls in BFO are shown in the bottom row.

Electrostatic potential inside the ferroelectric film satisfies the Poisson equation, $\varepsilon_0\varepsilon_b\Delta\varphi - \operatorname{div}\vec{P} = 0$, and the Laplace equation is valid in the dielectric gap; i.e., $\varepsilon_0\varepsilon_e\Delta\varphi = 0$ ($\varepsilon_e$ is the dielectric permittivity of external media). Electric boundary conditions are zero electric potential at the bottom of the film contacting the conducting substrate, $\varphi|_{x_3=0} = 0$, and the potential continuity, $\varphi|_{x_3=h-0} - \varphi|_{x_3=h+0} = 0$, at the interface between the ferroelectric film and the ambient medium. Another boundary condition at interface $x_3 = h$ is for the normal components of the electric displacement, namely, $D_3|_{x_3=h+0} - D_3|_{x_3=h-0} = \sigma(\varphi)|_{x_3=h}$ where $D_3 = P_3 - \varepsilon_0\varepsilon_b\frac{\partial\varphi}{\partial x_3}$ in the film, $(0 < x_3 < h)$ and $D_3 = -\varepsilon_0\varepsilon_e\frac{\partial\varphi}{\partial x_3}$ in the dielectric gap $(h < x_3)$. Here, we consider the special case of the surface screening charge with the density given by the expression $\sigma\ (\varphi) = -\varepsilon_0\varphi/\Lambda$, where $\Lambda$ is the effective screening length [85,86]. Typically the value of $\Lambda$ is smaller or even significantly smaller than 1 nm [87,88]. The condition $\Lambda \to 0$ corresponds to the perfect electric contact between the top conducting electrode and the film [89], and we consider the limit for comparison. The top electrode can be either biased $(\phi|_{x_3=h} = U)$ or grounded $(\phi|_{x_3=h} = 0)$, depending on the experimental situation corresponding to the scanning probe microscope tip placed on the film surface.

Elastic problem formulation is based on the modified Hooke's law obtained using the thermodynamic relation $u_{ij} = -\frac{\delta G_\sigma}{\delta \sigma_{kl}}$, where $u_{ij}$ are the components of the elastic strain tensor. Mechanical equilibrium conditions are $\partial\sigma_{ij}/\partial x_j = 0$ [90]. Note that the film-substrate interface was considered as an unstrained one (misfit strain is zero) corresponding to the elastically matched substrate.

The system of coupled Euler-Lagrange equations allowing for Khalatnikov relaxation of the oxygen tilt and polarization components, $\Phi_i$ and $P_i$, is

$$\frac{\delta G}{\delta P_i} = -\Gamma_P\frac{\partial P_i}{\partial t} \quad \text{and} \quad \frac{\delta G}{\delta \Phi_i} = -\Gamma_\Phi\frac{\partial \Phi_i}{\partial t}. \quad (7a)$$

These equations are supplemented by the boundary conditions of zero generalized fluxes at the film boundaries,

$$b^{(S)}\Phi_i + v_{ijkl}\frac{\partial \Phi_j}{\partial x_k}n_l\bigg|_S = 0,$$

$$a^{(S)}P_i + g_{ijkl}\frac{\partial P_j}{\partial x_k}n_l\bigg|_S = 0 \quad i = (1, 2, 3). \quad (7b)$$

The so-called "natural boundary conditions" for the tilt, $v_{ijkl}\frac{\partial \Phi_j}{\partial x_k}n_l|_S = 0$, correspond to $b^{(S)} = 0$, and the natural boundary conditions for polarization, $g_{ijkl}\frac{\partial P_j}{\partial x_k}n_l|_S = 0$, correspond to $a^{(S)} = 0$ in Eq. (7b). The natural conditions, which will be used hereinafter, correspond to the absence of surface energy (6) [91]. The explicit form of the free energy (1)–(6), Euler-Lagrange equations (7a) with boundary conditions (7b), are listed in the Supplemental Material [52].

TABLE I. BFO parameters used in LGD calculations (taken from Refs. [63,76]).

| Parameter | Designation | Numerical value for BFO |
|---|---|---|
| Background permittivity | $\varepsilon_b$ | 7 |
| Dielectric stiffness | $a_T$ ($\times 10^5$ C$^{-2}$ Jm/K) | 9 |
| Curie temperature for $P$ | $T_C$ (K) | 1300 |
| Barrett temperature for $P$ | $T_{qP}$ (K) | 800 |
| Fourth-order coefficients in the polarization expansion | $a_{ij}$ ($\times 10^8$ C$^{-4}$ m$^5$ J) | $a_{11} = -13.5,\ a_{12} = 5$ |
| Sixth-order coefficients in the polarization expansion | $a_{ijk}$ ($\times 10^9$ C$^{-6}$ m$^9$ J) | $a_{111} = 11.2,\ a_{112} = -3,\ a_{123} = -6$ |
| Electrostriction | $Q_{ij}$ (C$^{-2}$ m$^4$) | $Q_{11} = 0.03,\ Q_{12} = -0.01,\ Q_{44} = 0.01$ |
| Rotostriction | $R_{ij}$ ($\times 10^{18}$ m$^{-2}$) | $R_{11} = -1.32,\ R_{12} = -0.43,\ R_{44} = 8.45$ |
| Compliances | $s_{ij}$ ($\times 10^{-12}$ Pa$^{-1}$) | $s_{11} = 8.3,\ s_{12} = -2.7,\ s_{44} = 9.25$ |
| Polarization gradient coefficients | $g_{ij}$ ($\times 10^{-10}$ C$^{-2}$ m$^3$ J) | $g_{11} = 5,\ g_{12} = -0.5,\ g_{44} = 0.5$ |
| AFD-FE coupling | $\times 10^{29}$ C$^{-2}$ m$^{-2}$ J/K | $\xi_{11} = -0.5, \xi_{12} = 0.5, \xi_{44} = -2.6$ |
| Second-order coefficients in the tilt expansion | $b_T$ [$\times 10^{26}$ J/(m$^5$ K)] | 4 |
| Curie temperature for $\Phi$ | $T_\Phi$ (K) | 1440 |
| Barrett temperature for $\Phi$ | $T_{q\Phi}$ (K) | 400 |
| Fourth-order coefficients in the tilt expansion | $b_{ij}$ [$\times 10^{48}$ J/(m$^7$)] | $b_{11} = -24 + 4.5\,[\coth(300/T) - \coth(3/14)]$<br>$b_{12} = 45 - 4.5\,[\coth(300/T) - \coth(1/4)]$ |
| Sixth-order coefficients in the tilt expansion | $b_{ijk}$ [$\times 10^{70}$ J/(m$^9$)] | $b_{111} = 4.5 - 3.4\,[\coth(400/T) - \coth(2/7)]$<br>$b_{112} = 3.6 - 0.04\,[\coth(10/T) - \coth(1/130)]$<br>$b_{123} = 41 - 43.2\,[\coth(1200/T) - \coth(12/11)]$ |
| Tilt gradient coefficients | $v_{ij}$ ($\times 10^{11}$ J/m$^3$) | $\nu_{11} = 0.25,\ \nu_{44} = (0.25 - 25)$ |
| Polarization extrapolation length | $\lambda_i^P \equiv g_{i3}^{(P)}/a_i^{(S)}$ (nm) | Varied from zero to high $h$ values $> 100$ nm |
| Tilt extrapolation length | $\lambda_i^\Phi \equiv v_{i3}^{(\Phi)}/b_i^{(S)}$ (nm) | Varied from zero to high $h$ values $> 100$ nm |
| Effective screening length | $\Lambda$ (nm) | Varied from zero to 0.1 nm, $\Lambda = 0$ in Figs. 3–12. |

### C. Impact of biquadratic coupling on the stability of homogeneous *R*3*c* phase

Experimentally, bulk BFO should be in a rhombohedral $R3c$ phase at temperatures below $T_C$. Since the biquadratic coupling and gradient energy coefficients in the free energy (1)–(5) are poorly known, one should be very careful with the choice of their numerical values in order to prevent the appearance of so-called nonphysical "extra" phases [63], which do not exist in reality and should be eliminated from the theoretical analysis of the domain structure configuration. Therefore, priory to studying the effect of the gradient energy on domain structure, let us analyze whether any extra phase can be (meta)stable below $T_C$ for a chosen free energy functional form (1)–(5) with parameters taken from Refs. [63,76] and listed in Table I. For this purpose let us perform the following analytical and numerical calculations.

Without biquadratic coupling contribution, i.e., for $\Delta G_{\mathrm{BQC}} = 0$, and neglecting the sixth powers of the polarizations and tilts, and their gradients, the energies of oxygen tilts and polarization are decoupled, and, using the idea of Dzyaloshinsky substitution [92], one can introduce the new variables $\Phi^2 = \frac{\Phi_1^2+\Phi_2^2+\Phi_3^2}{\sqrt{3}}$, $\Psi^2 = \frac{\Phi_3^2-\Phi_1^2}{\sqrt{2}}$, and $\Omega^2 = \frac{2\Phi_2^2-\Phi_1^2-\Phi_3^2}{\sqrt{6}}$, which diagonalize the AFD contribution to the free energy. Similar substitution for polarization components, $P^2 = \frac{P_1^2+P_2^2+P_3^2}{\sqrt{3}}$, $Q^2 = \frac{P_3^2-P_1^2}{\sqrt{2}}$, and $R^2 = \frac{2P_2^2-P_1^2-P_3^2}{\sqrt{6}}$, diagonalizes the FE energy. Namely,

$$\Delta G_{\mathrm{AFD}}^{2-4}[\Phi, \Psi, \Omega] = \sqrt{3}b_1\Phi^2 + (b_{11} + b_{12})\Phi^4 + \left(b_{11} - \frac{b_{12}}{2}\right)(\Psi^4 + \Omega^4), \tag{8a}$$

$$\Delta G_{\mathrm{FE}}^{2-4}[P, Q, R] = \sqrt{3}a_1 P^2 + (a_{11} + a_{12})P^4 + \left(a_{11} - \frac{a_{12}}{2}\right)(Q^4 + R^4). \tag{8b}$$

Expressions (8a) and (8b) have the four global equivalent minimums in the AFD-FE phase, which are stable at $b_1 < 0$, $b_{11} - \frac{b_{12}}{2} > 0$, $a_1 < 0$, and $a_{11} - \frac{a_{12}}{2} > 0$. The coordinates of the minimums in the six-dimensional (6D) phase space are

$$\{\Phi,\ \Psi,\ \Omega, P,\ Q,\ R\} = \left\{\pm\sqrt{-\frac{\sqrt{3}b_1}{2(b_{11}+b_{12})}},\ 0,\ 0,\ \pm\sqrt{-\frac{\sqrt{3}a_1}{2(a_{11}+a_{12})}},\ 0,\ 0\right\}. \tag{9}$$

Each of the minimums corresponds to the conventional $R3c$ phase of BFO, in which $\Phi_1^2 = \Phi_2^2 = \Phi_3^2 = -\frac{b_1}{2(b_{11}+b_{12})}$ and $P_1^2 = P_2^2 = P_3^2 = -\frac{a_1}{2(a_{11}+a_{12})}$.

Nonzero biquadratic coupling energy $\zeta_{ijkl}\Phi_i\Phi_j P_k P_l$ given by Eq. (4), as well as sixth-order powers $\Phi_i^6$ and $P_i^6$ included in Eqs. (2) and (3), make the diagonalization (8) impossible. The minimums can be shifted, and, moreover, some of them can become metastable or even disappear due to the biquadratic coupling and sixth-order terms contribution. Specifically, in coordinates $\{\Phi,\ \Psi,\ \Omega, P,\ Q,\ R\}$ the "isotropic" part of biquadratic energy $\Delta G^{11}_{\rm BQC}$ can be identically rewritten as

$$\Delta G^{11}_{\rm BQC} = \zeta_{11}\left(\Phi_1^2P_1^2 + \Phi_2^2P_2^2 + \Phi_3^2P_3^2\right) \equiv \zeta_{11}(\Phi^2P^2 + \Psi^2Q^2 + \Omega^2R^2). \tag{10}$$

The oversimplified free energy (7) and (8) including the isotropic biquadratic coupling energy (10) has the form

$$\Delta G^{2-4}_{\rm AFD-FE} = \left[\sqrt{3}b_1\Phi^2 + (b_{11}+b_{12})\Phi^4 + \left(b_{11} - \frac{b_{12}}{2}\right)(\Psi^4+\Omega^4) + \sqrt{3}a_1P^2 \right.$$
$$\left. + (a_{11}+a_{12})P^4 + \left(a_{11} - \frac{a_{12}}{2}\right)(Q^4+R^4) + \zeta_{11}(\Phi^2P^2 + \Psi^2Q^2 + \Omega^2R^2)\right]. \tag{11}$$

The energy (11) has four energetically equivalent minimums with coordinates

$$\{\Phi,\ \Psi,\ \Omega, P,\ Q,\ R\} = \left\{\pm\sqrt{\frac{\sqrt{3}[a_1\zeta_{11} - 2b_1(a_{11}+a_{12})]}{4(b_{11}+b_{12})(a_{11}+a_{12}) - \zeta_{11}^2}},\ 0,\ 0,\ \pm\sqrt{\frac{\sqrt{3}[b_1\zeta_{11} - 2a_1(b_{11}+b_{12})]}{4(a_{11}+a_{12})(b_{11}+b_{12}) - \zeta_{11}^2}},\ 0,\ 0\right\}. \tag{12}$$

These minimums correspond to the $R3c$ phase in a bulk AFD-FE multiferroic with isotropic biquadratic coupling. Unfortunately, we could not find any analytical expressions for the minimum coordinates if the anisotropic biquadratic coupling (4) is included in the free energy (1).

Calculations were performed for the 2-4-6 coupled free AFD-FE energy (1)–(5) with BFO parameters from Table I. Cross sections of the free energy surface have been calculated without [$\zeta_{ijkl} = 0$, Fig. 2(a)] and with [$\zeta_{ijkl} \neq 0$, Fig. 2(b)] biquadratic coupling energy (4). The differences between Figs. 2(a) and 2(b) are caused by isotropic terms $\zeta_{11}(\Phi_1^2P_1^2 + \Phi_2^2P_2^2 + \Phi_3^2P_3^2)$ in Eq. (10) and anisotropic terms $\zeta_{44}(\Phi_1\Phi_2P_1P_2 + \Phi_2\Phi_3P_2P_3 + \Phi_1\Phi_3P_1P_3)$ in Eq. (4). Four equivalent deepest minimums with nonzero coordinates $\Phi_1 = \Phi_2 = \Phi_3 \neq 0$ and $P_1 = P_2 = P_3 \neq 0$, and zero coordinates $\Psi = \Omega = Q = R = 0$, are seen in Figs. 2(a) and 2(b) [see also Eq. (9)]. The minimums are separated by a local maximum at the coordinate origin and four saddle points. The case $\Phi_1^2 = \Phi_2^2 = \Phi_3^2$, $P_1^2 = P_2^2 = P_3^2$, and $\Psi = \Omega = Q = R = 0$ corresponds to the stable $R3c$ phase.

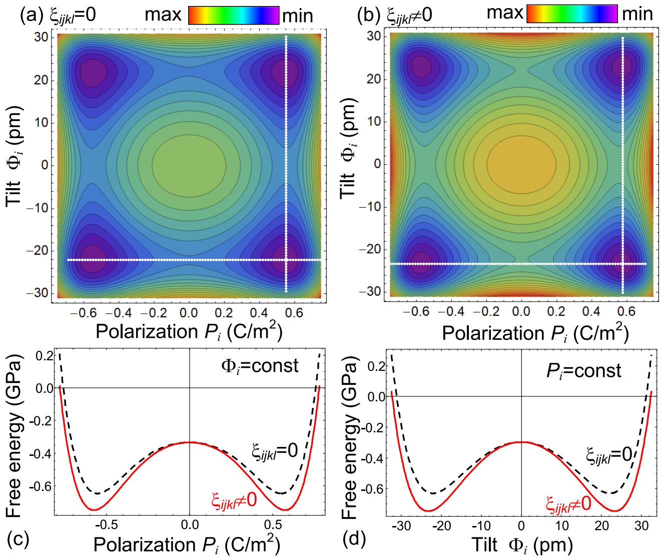

FIG. 2. Free energy dependence on the tilt and polarization components, $\Phi_i = \Phi_1 = \Phi_2 = \Phi_3$ and $P_i = P_1 = P_2 = P_3$. Contour maps were calculated at room temperature without (a) and with (b) biquadratic coupling contribution. The free energy dependence on $\Phi_i$ at fixed $P_i = 0.48\,\mathrm{C/m^2}$ (c), and its dependence on $P_i$ at fixed $\Phi_i = 22\,\mathrm{pm}$ (d). Dashed and solid curves in plots (c,d) show the cases without ($\zeta_{ijkl} = 0$) and with ($\zeta_{ijkl} \neq 0$) biquadratic coupling contribution, respectively. Corresponding cross sections are shown by white lines in plots (a,b). BFO parameters are listed in Table I; $T = 300\,\mathrm{K}$.

The free energy dependence on polarization at fixed tilt components, $\Phi_i = \Phi_1 = \Phi_2 = \Phi_3 = 22\,\mathrm{pm}$, and the dependence of the energy on the tilt at fixed polarization components, $P_i = P_1 = P_2 = P_3 = 0.48\,\mathrm{C/m^2}$, are shown in Figs. 2(c) and 2(d), respectively. The influence of the coupling makes the minimums deeper, but does not shift or eliminate them [compare solid and dashed curves in Figs. 2(c) and 2(d)].

We checked numerically that any other local (or global) minimums corresponding to nonzero coordinates $\{P, \Phi, \Psi,\ \Omega,\ Q,\ R\}$ is absent for the BFO parameters listed in Table I. Hence among all homogeneous phases, only the $R3c$ phase is absolutely stable below $T_C$ in bulk BFO without polarization or tilt gradient energy. The result is expected and confirms the appropriate choice of the free energy form given by Eqs. (1)–(5) and numerical parameters in Table I. That is why we can conclude that any other metastable or stable phases or/and domain configurations, different from $R3c$, which will be revealed and analyzed in the next sections, cannot originate from the "extra" local minimums of the free energy (1)–(5).

The values of the flexoelectric tensor components $F_{ijkl}$ are not listed in Table I due to their small impact on the studied phenomena. We vary them within typical range $0 \leqslant |F_{ijkl}| \leqslant 10^{-11}\,\mathrm{m^3/C}$.

## III. SIMULATION RESULTS AND DISCUSSION

### A. Simulation details

We used FEM to simulate the oxygen tilt and polarization distributions in thin freestanding BFO films covered by conducting electrodes. The film thickness $h$ varied from 5 to 500 nm, and the typical picture of domain morphology was observed at $h > 15\,\mathrm{nm}$; so we use the thicknesses (16–20) nm for illustration. BFO parameters used in the FEM calculations to generate figures are listed in Table I.

The values of $a^{(S)}$ and $b^{(S)}$ in the boundary conditions (7b) significantly affect the "critical thickness" of the film [91].

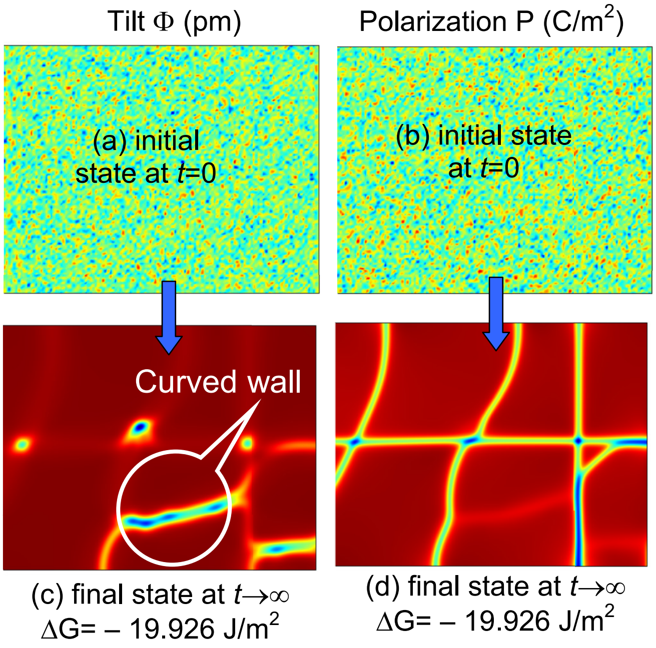

FIG. 3. Initial random seeding and final distributions of the tilt (a,c) and polarization (b,d) calculated in a 16-nm BFO film. Gradient coefficient $\nu_{44} = 0.25 \times 10^{11}\,\mathrm{J/m^3}$; $T = 300\,\mathrm{K}$; other parameters are listed in Table I.

The critical thickness is the thickness below which the size-induced phase transition to a parent (e.g., paraelectric) phase without long-range order occurs (see, e.g., Refs. [91,93]). As it follows from the analytical expressions derived in Refs. [47,91] the critical thickness of FE (or AFD) transition decreases with $a^{(S)}$ (or $b^{(S)}$) increase, so that the application of the natural boundary conditions ($a^{(S)} = b^{(S)} = 0$) leads to the minimal critical thickness of the film (see, e.g., [47,91]).

To minimize the influence of the surface on the obtained results, we put $a^{(S)} = b^{(S)} = 0$ in the boundary conditions (7b). For comparison we performed simulations for zero polarization and tilt components at the film surfaces, $P_i|_{x_3=0,h} = 0$ and $\Phi_i|_{x_3=0,h} = 0$, which correspond to the maximal influence of the surface. These conditions lead to the maximal critical thickness of the film [47,91].

It appeared that curved walls arise as a result of the relaxation process of a random domain distribution, named "random seeding" (see Fig. 3). Also the random seeding can be superimposed on the ideal nominally uncharged 180°, 109°, and 71° domain wall structure in the $R3c$ phase. Initial and final domain states are shown in Fig. 4 and in Fig. S2 in the Supplemental Material [52].

From Figs. 3, 4, and S2 [52] the "curved," "meandering," and "zigzaglike" features appeared at the 180° and 109° AFD walls, but not at the 71° walls. Schematic images of the straight, curved, meandering, and zigzaglike domain wall profiles are shown in Fig. S1 in the Supplemental Material [52].

The energy density excesses $\Delta G$ corresponding to the relaxation of the initial random domain distribution (RD); polydomain distribution (PD) with straight 180°, 109°, and 71° domain walls; and polydomain distribution disturbed by a random seeding (PD + RD) have been compared. It appeared that the energies are surprisingly close, namely, $\Delta G = -19.926\,\mathrm{J/m^2}$ for the curved domain walls obtained from the relaxation of RD (see Fig. 3), $\Delta G = -19.853\,\mathrm{J/m^2}$ for the 180° domain walls obtained from the relaxation of PD+RD [see Figs. 4(a)–4(d)], and $\Delta G = -19.865\,\mathrm{J/m^2}$ for the 180° domain walls obtained from the relaxation of PD [see Figs. 4(e) and 4(f)]. The final distributions of the polarization and tilt shown in Figs. 3 and 4, which have high negative and approximately equal energies $\Delta G \approx -19.9\,\mathrm{J/m^2}$, are long-living metastable states of the curved domain walls in BFO [94].

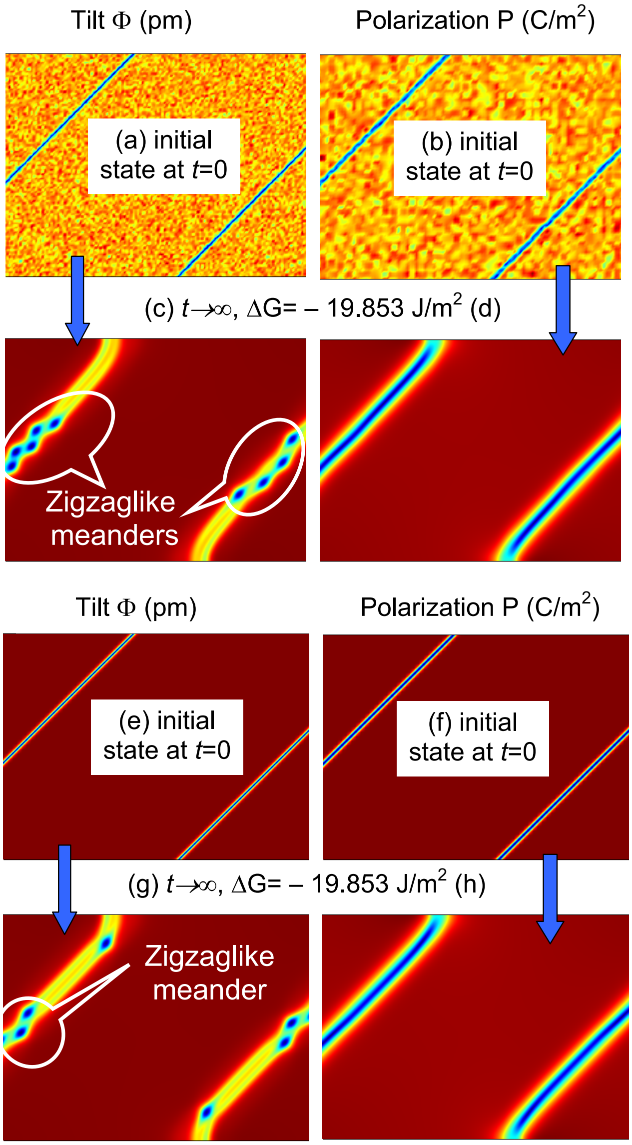

FIG. 4. Initial and final distributions of the tilt (a,c) and polarization (b,d) calculated in a 16-nm BFO film. The 180° domains were imposed on random seeding. Gradient coefficient $\nu_{44} = 0.25 \times 10^{11}\,\mathrm{J/m^3}$; $T = 300\,\mathrm{K}$; other parameters are listed in Table I.

From the analysis of the free energy relief presented in Sec. II C we cannot establish the origin of the curved, meandering, and zigzaglike AFD-FE walls shown in Figs. 3(c), 3(d), 4(c), and 4(g), so what is the physical origin of the

TABLE II. AFD and FE order parameter correlation lengths $L_C^\Phi$ and $L_C^P$ in BFO.

| Order parameter | Type of uncharged domain wall | | |
|---|---|---|---|
| | 180° | 109° | 71° |
| $\Phi_1$ | $L_C^\Phi = \sqrt{\frac{v_{11}+v_{12}+2v_{44}}{-4b_1}} = 3.72$ Å | Nonapplicable, since $\Phi_1 \approx$ const. | Non applicable, since $\Phi_1 \approx$ const. |
| $\Phi_2$ | $L_C^\Phi = \sqrt{\frac{v_{44}}{-2b_1}} = 1.75$ Å | $L_C^\Phi = \sqrt{\frac{v_{44}}{-2b_1}} = 1.75$ Å | Nonapplicable, since $\Phi_2 \approx$ const. |
| $\Phi_3$ | $L_C^\Phi = \sqrt{\frac{v_{11}-v_{12}}{-4b_1}} = 0.78$ Å | $L_C^\Phi = \sqrt{\frac{v_{44}}{-2b_1}} = 1.75$ Å | $L_C^\Phi = \sqrt{\frac{v_{44}}{-2b_1}} = 1.75$ Å |
| $P_1$ | $L_C^P = \sqrt{\frac{g_{11}+g_{12}+2g_{44}}{-4a_1}} = 6.20$ Å | Nonapplicable, since $P_1 \approx$ const. | Nonapplicable, since $P_1 \approx$ const. |
| $P_2$ | $L_C^P = \sqrt{\frac{g_{44}}{-2a_1}} = 2.38$ Å | $L_C^P = \sqrt{\frac{g_{44}}{-2a_1}} = 2.38$ Å | Nonapplicable, since $P_2 \approx$ const. |
| $P_3$ | $L_C^P = \sqrt{\frac{g_{11}-g_{12}}{-4a_1}} = 4.87$ Å | $L_C^P = \sqrt{\frac{g_{44}}{-2a_1}} = 2.38$ Å | $L_C^P = \sqrt{\frac{g_{44}}{-2a_1}} = 2.38$ Å |

meandering 180° and 109° domain boundaries? Why does the effect not exist at 71° domain walls? To establish the origin, we performed the following numerical experiments.

(a) The unusual meandering AFD-FE domain structures exist and become insensitive to the screening length values at $\Lambda \ll 0.1$ nm. We observed the stable meandering domains in the limiting case $\Lambda \to 0$ corresponding to perfect screening and minimal depolarization electric field. Hence the origin of the meandering walls is not the incomplete screening of ferroelectric polarization by the imperfect electrodes or surface charge. Therefore the low

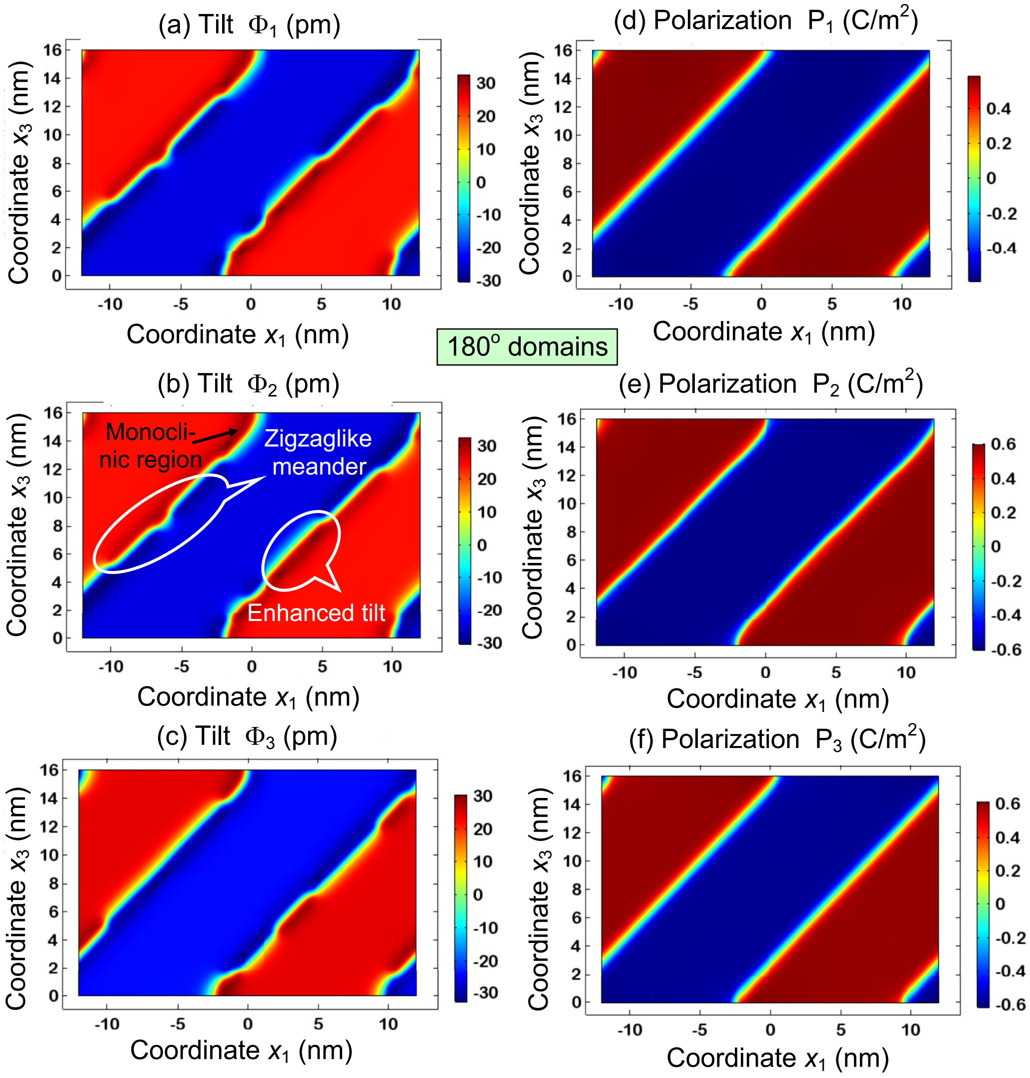

FIG. 5. Distribution of the tilt $\Phi_i$ (a–c) and polarization $P_i$ (d–f) components calculated for the case of 180° domains in a 16-nm BFO film. Gradient coefficient $v_{44} = 2.5 \times 10^{10}\,\mathrm{J/m^3}$; $T = 300$ K; other parameters are listed in Table I.

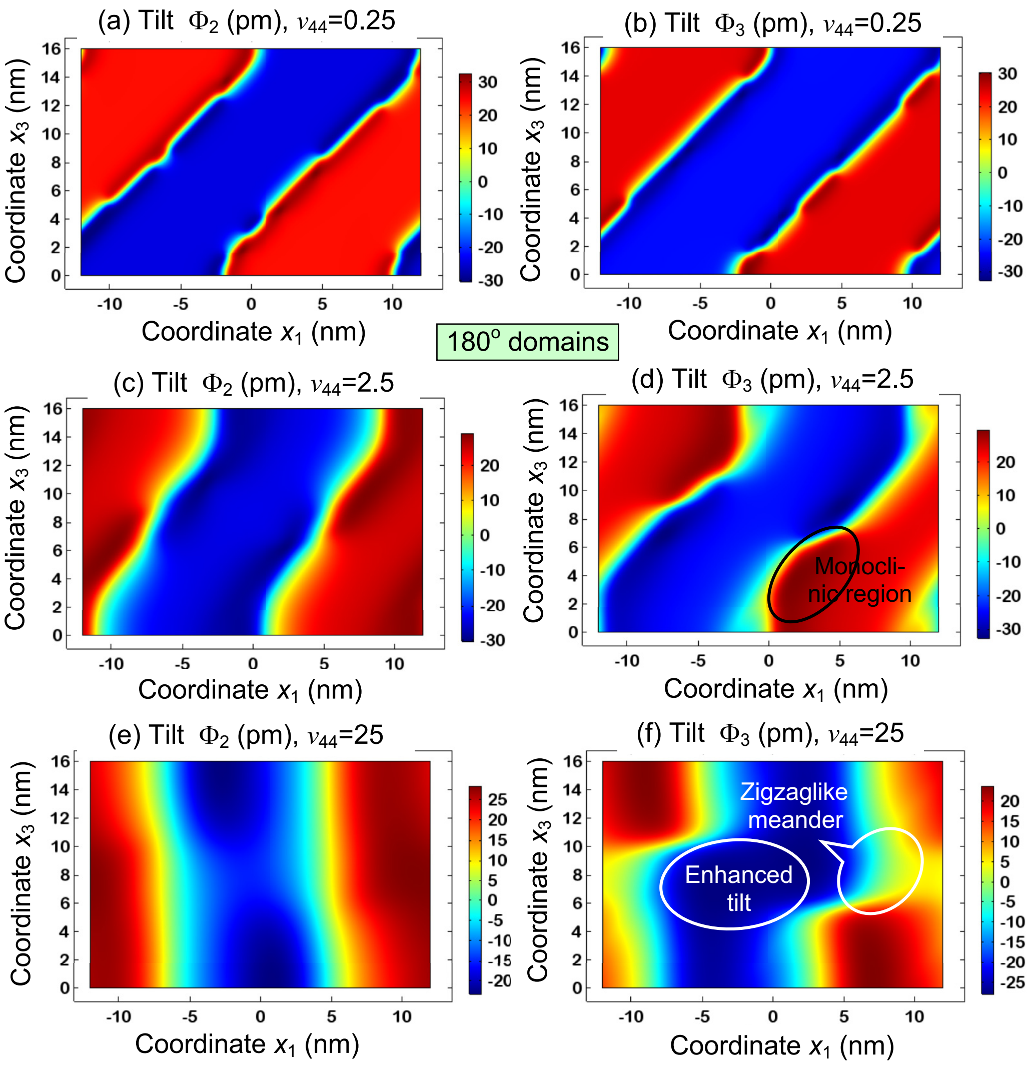

FIG. 6. Distribution of the tilt components $\Phi_2$ (a,c,e) and $\Phi_3$ (b,d,f) calculated for the case of 180° domains in a thin BFO film. The gradient coefficient $v_{44} = 2.5 \times 10^{10}\,\mathrm{J/m^3}$ (a,b), $2.5 \times 10^{11}\,\mathrm{J/m^3}$ (c,d), and $2.5 \times 10^{12}\,\mathrm{J/m^3}$ (e,f). $T = 300\,\mathrm{K}$; other parameters are listed in Table I.

symmetry domains limited by the meandering walls are quite possible.

(b) We explored whether the meandering walls originate from the spatial confinement of polarization components at the film surfaces. That is, we compared the changes of the AFD-FE domain morphology when the polarization extrapolation lengths $\lambda_i^P \equiv \frac{g_{i3}^{(P)}}{a_i^{(S)}}$ vary from 0 (corresponding to zero polarization at the film surfaces, $P_i|_{x_3=0,h} = 0$) to infinity (corresponding to $a_i^{(S)} = 0$ and $\frac{\partial P_i}{\partial x_3}|_{x_3=0,h} = 0$). For $\lambda_i^P = 0$ we see the appearance of FE domain wall broadening at the surface and its gradual decrease with $\lambda_i^P$ increasing, as anticipated. However no significant changes of the meandering walls occur in the film with $\lambda_i^P$ changing.

(c) We further compared the changes of the AFD-FE domain structure when the tilt extrapolation lengths $\lambda_i^\Phi \equiv \frac{v_{i3}^{(\Phi)}}{b_i^{(S)}}$ vary from 0 (corresponding to zero polarization at the film surfaces, $\Phi_i|_{x_3=0,h} = 0$) to infinity (corresponding to $b_i^{(S)} = 0$ and $\frac{\partial \Phi_i}{\partial x_3}|_{x_3=0,h} = 0$). For $\lambda_i^\Phi = 0$ we see the appearance of AFD domain wall broadening at the surface and its gradual decrease with $\lambda_i^\Phi$ increasing. However, no significant changes of the domain morphology occur with $\lambda_i^\Phi$ changing. Further we can assume that the spatial confinement delineates the appropriate boundary conditions for the oxygen tilt and polarization components at the film surfaces.

(d) We rotate the film surface cut to find the angle for which both AFD and FE walls are straight without inclusion of any other phases. We made sure that the angle does not exist. Also, we checked whether the meandering walls originate from the spatial confinement effect delineated by the appropriate boundary conditions for the oxygen tilt at the film surfaces. We increase the film thickness up to 500 nm and see that no significant changes in the morphology of meandering domains occur.

(e) Finally, we varied the components of the electrostrictive and flexoelectric couplings tensors in a typical range ($0 \leqslant |F_{ijkl}| \leqslant 10^{-11}\,\mathrm{m^3/C}$, $0 \leqslant |Q_{ijkl}| \leqslant 0.1\,\mathrm{m^4/C^2}$), and lead to the conclusion that the appearance of observed effects do not stem from the couplings, because the meandering

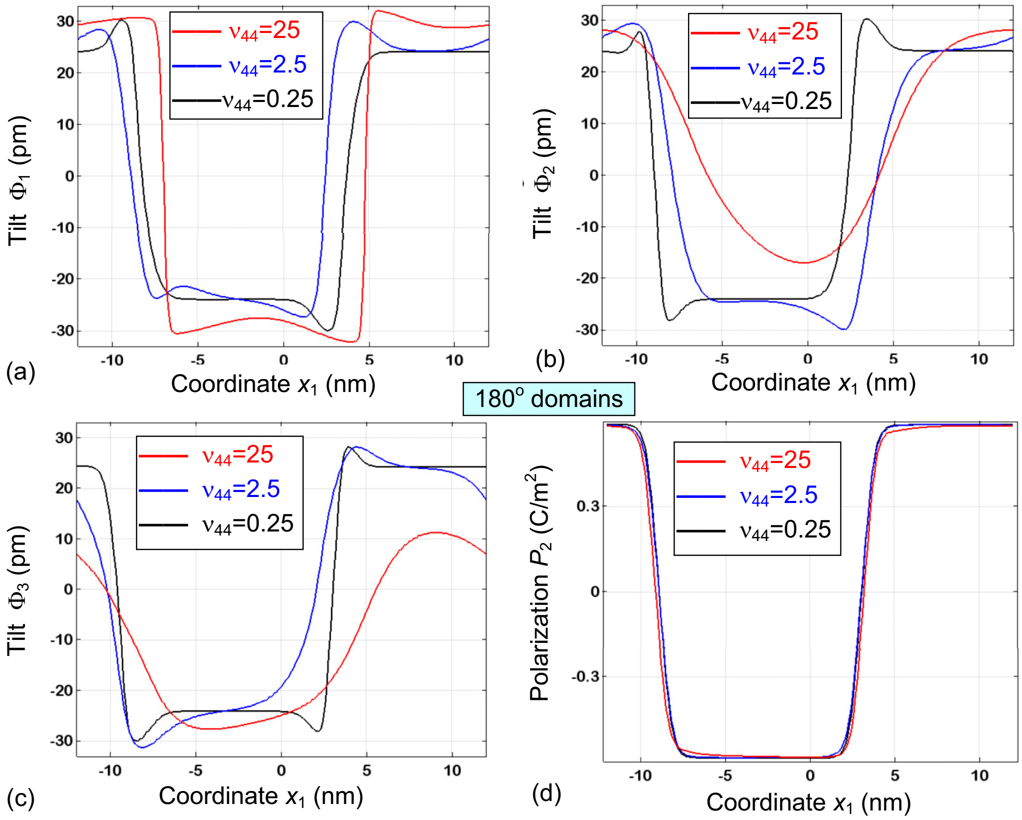

FIG. 7. Profiles of the tilt components $\Phi_i$ (a,b,c), and polarization $P_2$ (d) calculated for the case of 180° domains in the middle of 16-nm BFO film ($x_3 = h/2$) at room temperature. The gradient coefficient $\nu_{44} = 0.25 \times 10^{11}$ J/m$^3$ (black curves), $2.5 \times 10^{11}$ J/m$^3$ (blue curves), and $25 \times 10^{11}$ J/m$^3$ (red curves); $T = 300$ K; other parameters are listed in Table I.

AFD walls weakly react on the changes of $F_{ijkl}$ and $Q_{ijkl}$ values.

(f) It appeared that the change of the tilt gradient coefficients $v_{ijkl}$ significantly affects the curvature and meandering of domain walls, including the monoclinic phase appearance at the curved walls. It is important to underline that the monoclinic phase can be stable in a ferroic with one vectorial long-range order parameter, e.g., in a "normal" ferroelectric with a polarization vector **P**, if the higher-order powers of **P** (from eighth to 12th) are included in the LGD free energy [95]. As a matter of fact, we consider two vectors, **P** and **Φ**, as the long-range order parameters, using 2-4-6 LGD expansion for each of them in numerical modeling [see Eqs. (2) and (3) and Table I], and simplified 2-4 expansion in analytical calculations [see Eqs. (8a) and (8b)]. Hence the effective order of the nonlinearity in the coupled Euler-Lagrange equations for **P** and **Φ** is 12 for numerical calculations and 8 for analytical calculations, making the appearance of monoclinic phases quite possible. Earlier we had found that the monoclinic phase can be stabilized without the eighth powers of polarization, if the coupling between **P** and **Φ** is included [34].

(g) The impact of the polarization gradient coefficients $g_{ijkl}$ is much less pronounced, because the FE walls do not bend in order to remain uncharged. The charging of the FE wall by the polarization bound charge will immediately lead to the appearance of a strong depolarization electric field $E_i^d$ ($\text{div}\vec{E}^d \sim -\text{div}\vec{P}$); that is, energy excess $-E_i^d P_i/2$ is positive at the region of the curved wall and relatively high. Thus, the polarization subsystem behaves in such a way to prevent the charging.

From the analysis of (a)–(g) we concluded that the origin of meandering AFD-FE domain walls is the coupling between the tilts and polarization gradient coefficients. This conclusion is consistent with the results of Conti *et al.* [96] for multiferroics with symmetric free energy and two order parameters. Conti *et al.* used a simple phenomenological model and have shown that the maximum and minimum near the antiphase domain walls appear on the profile of one of the order parameters depending on the anisotropy gradient energy, in the mixed phase when both order parameters are nonzero. Despite the fact that we consider a much more complex system with six order parameters, the extremums observed near the domain walls are qualitatively similar to the ones predicted by Conti *et al.* Thus, the appearance of maximums and minimums on the profiles of the order parameters near the domain walls can be associated with the features (such as anisotropy) of the gradient energy.

To quantify the statement, one can introduce the tilt correlation length $L_C^\Phi \sim \sqrt{v}$ that is defined from the correlation function of the tilt vector fluctuations. The correlation length of polarization fluctuations $L_C^P \sim \sqrt{g}$ can be introduced in a conventional way (see, e.g., Ref. [18]). Note that correlation lengths $L_C^\Phi$ and $L_C^P$ determine the width of the AFD and FE domain walls [18]. Since the correlation function depends

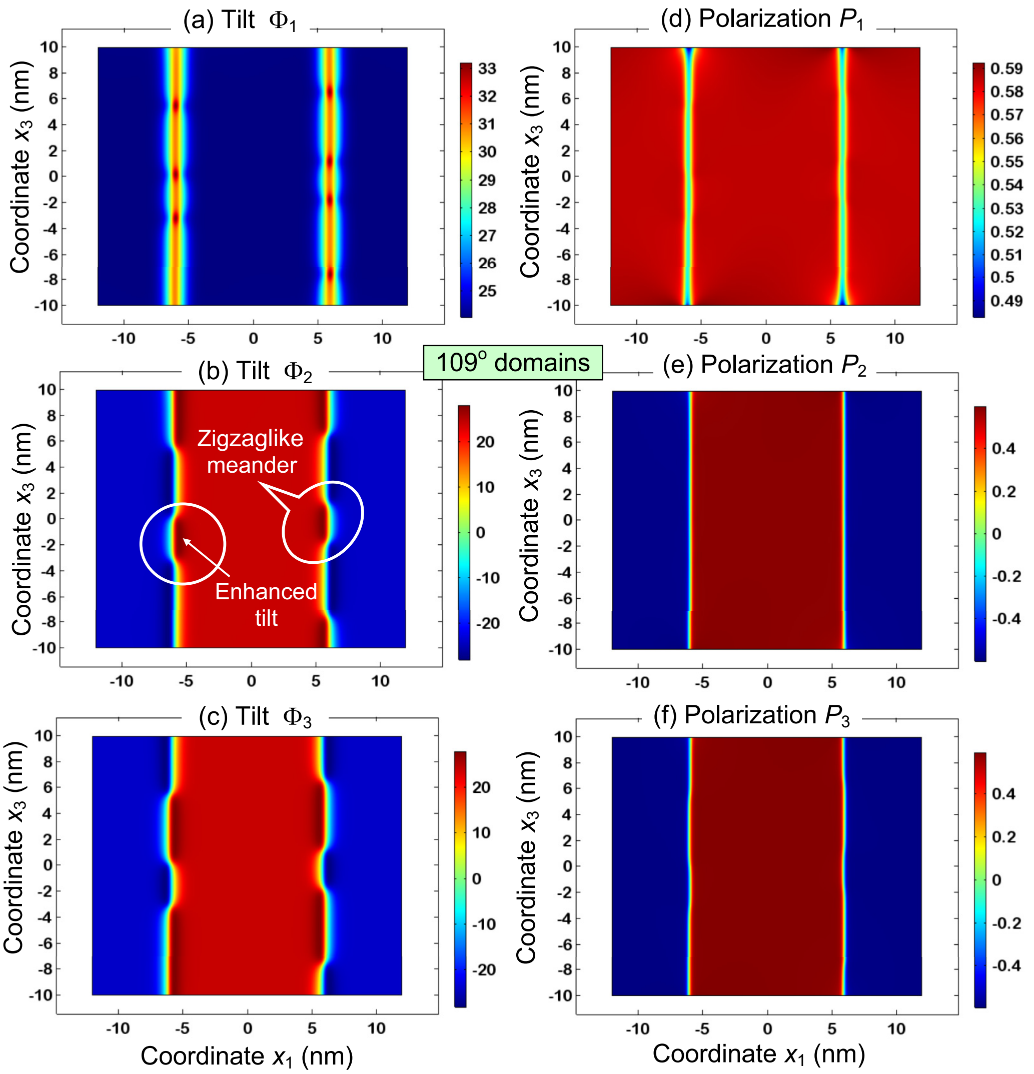

FIG. 8. Distribution of the AFD order parameter $\Phi_i$ (a–c) and polarization $P_i$ (d–f) calculated for the case of 109° domains in a thin BFO film. $T = 300$ K; BFO parameters are listed in Table I.

both on the wave vector of fluctuations and their orientation in **r** space, it is anisotropic. In other words, the correlation function of tilt (or polarization) fluctuations is the second rank tensor. Table II lists the analytical expressions and numerical values of correlation lengths for the tilt and polarization vector components. It is seen that $L_C^\Phi$ varies significantly at the 180° domain wall for the different tilts (from 3.72 Å for $\Phi_1$ to 0.78 Å for $\Phi_3$), and $L_C^P$ varies from 6.20 Å for $P_1$ to 2.38 Å for $P_2$ components. The tilt and polarization changes at the 109° domain wall behave as in the hypothetic "isotropic" ferroic, namely, $L_C^\Phi = 1.75$ Å for both tilt components and $L_C^P = 1.75$ Å for both polarizations. Contrarily, only the components $\Phi_3$ and $P_3$ vary across the 71° domain wall; therefore $L_C^\Phi = 1.75$ Å for $\Phi_3$ and $L_C^P = 2.38$ Å for $P_3$.

### B. Meandering 180° AFD-FE domain walls

Using FEM of the AFD and FE properties of strain-free thin BFO films, we further observe that the conventional 180° domains of bulk rhombohedral AFD-FE phase [see Fig. 1(a)] are separated by the zigzaglike meandering domain walls, which in fact contain thin AFD-FE domain regions of lower monoclinic symmetry and different parity (see Fig. 5).

The contrast of the monoclinic domains is determined by the magnitude of the tilt components $\Phi_i$; it is higher in the vicinity of the meandering walls in comparison with the contrast in the center of the 180° domain [see dark-red and dark-blue regions near meandering boundaries in Figs. 5(a)–5(c)]. Surprisingly, neither curvature nor enhanced contrast is inherent to the FE component of the 180° domain boundaries [see straight incline domain boundaries with gradually changing color from red to blue in Figs. 5(d)–5(f)]. Actually, the contrast enhancement in the meandering regions [marked by the ellipse in Fig. 5(b)] does not correspond to the bulk rhombohedral phase and represents itself the domains of lower monoclinic symmetry with $\Phi_1 \neq \Phi_2 \neq \Phi_3$ imposed on the 180° AFD-FE domains in the rhombohedral phase.

The influence of the tilt gradient coefficient $v_{44}$ on the domain structure can be seen from Figs. 6 and 7. Meandering AFD domain walls broaden significantly and decrease their

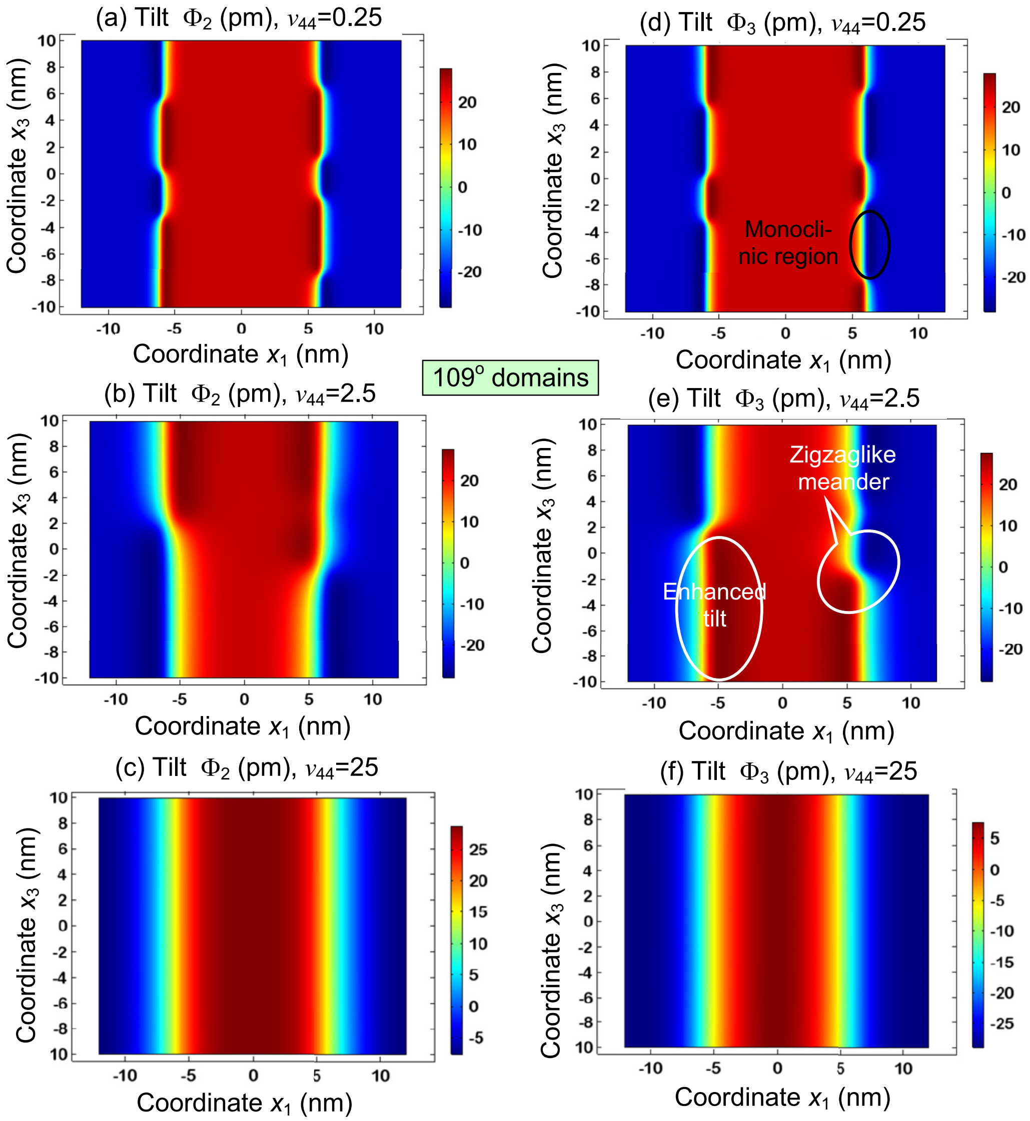

FIG. 9. Distributions of the tilt components $\Phi_2$ (a–c) and $\Phi_3$ (d–f) calculated for the case of 109° domains in a thin BFO film. The gradient coefficient $v_{44} = 0.25 \times 10^{11}\ \mathrm{J/m^3}$ (a,e), $0.5 \times 10^{11}\ \mathrm{J/m^3}$ (b,f), $1 \times 10^{11}\ \mathrm{J/m^3}$ (c,g), and $2 \times 10^{11}\ \mathrm{J/m^3}$ (d,h). $T = 300$ K; BFO parameters are listed in Table I.

curvature with an increase of $v_{44}$ by a factor of 10. In addition to significant broadening, a visible asymmetry of the wall profile appears with an increase of $v_{44}$ by a factor of 100. As one can see from the figures, the maximal deviation of the tilt from bulk value is dependent on $v_{44}$, but polarization profiles are almost independent of this parameter. Thus, we conclude that the appearance of meandering walls and low symmetry phases is conditioned by the decrease of the tilt gradient energy. If $v_{44}$ is sufficiently small, the energy increase associated with the AFD wall bending is less than the energy decrease associated with the terms proportional to $b_{ij}\Phi_i^2\Phi_j^2$.

### C. Meandering 109° AFD-FE domain walls

Rhombohedral 109° domains correspond to the case when two components of vectorial order parameter change its sign when crossing the wall plane [see Fig. 1(b)]. These are the components $\Phi_2$, $\Phi_3$ and $P_2$, $P_3$, respectively, for the 109° domains in BFO. These domains are separated by the AFD meandering domain walls, which in fact contain thin domains of lower symmetry [see Figs. 8(b) and 8(c)]. Enhanced contrast is also inherent to the FE component at the domain boundaries [see the boundaries with gradually changing color from red to blue in Figs. 8(a)–8(c)]. Actually, the contrast enhancement in the meandering regions does not correspond to the bulk rhombohedral $R3c$ phase. There are the domains of lower symmetry with $\Phi_1 \neq \Phi_2 \neq \Phi_3$ and $P_1 \neq P_2 \neq P_3$ imposed on the twin boundaries in the rhombohedral phase.

Similarly to the case of the low symmetry phases appearing in the vicinity of the meandering 180° AFD-FE domain walls (considered in Sec. III B) we made sure that the appearance of low symmetry domains at the 109° domain walls does not stem from the spatial confinement or imperfect screening of spontaneous polarization, electrostrictive or flexoelectric

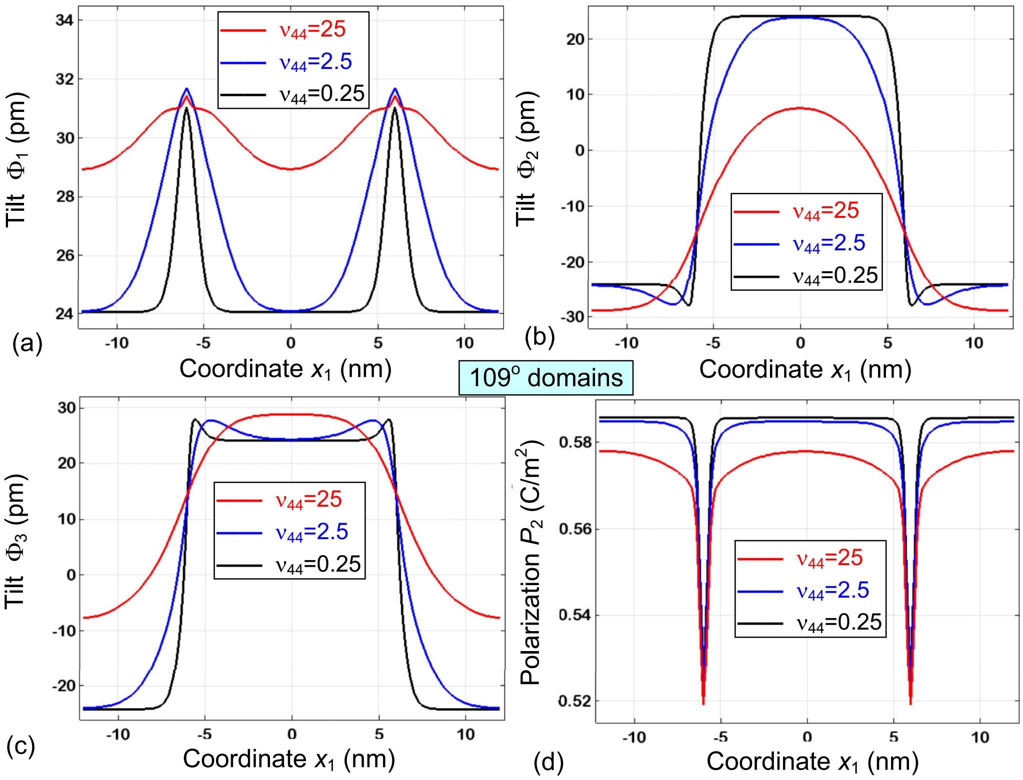

FIG. 10. Profiles of the tilt $\Phi_2$ (a–c), and polarization $P_2$ (d) calculated for the case of 109° domains in a 16-nm BFO film at room temperature. The gradient coefficient $\nu_{44} = 0.25 \times 10^{11}\ \mathrm{J/m^3}$ (black), $2.5 \times 10^{11}\ \mathrm{J/m^3}$ (blue), and $25 \times 10^{11}\ \mathrm{J/m^3}$ (red). $x_3 = h/2$; $T = 300\ \mathrm{K}$; BFO parameters are listed in Table I.

couplings, but rather from the interplay between the gradient of the oxygen tilt and polarization components at the domain walls. Indeed, the influence on the tilt gradient coefficient value is shown in Fig. 9. Distributions of order parameters in the central part of the film, corresponding to Fig. 9, are shown in Fig. 10.

One can see two tendencies with increase of $\nu_{44}$. The first tendency is an obvious increase of domain wall width (proportional to $\sqrt{\nu_{44}}$) and the second one is the decrease of the meandering walls' density and curvature, which separate monoclinic regions. As one can see from Fig. 10, the amplitude of the tilt deviation from the bulk value is independent of the gradient coefficient $\nu_{44}$. However, the low symmetry region occupies the central part of the BFO film for the high values of $\nu_{44}$. The regions are characterized by the different amplitudes of the tilt components near and far from the 109° domain walls.

### D. 71° AFD-FE domain walls

Bulk 71° domains correspond to the case when only one component of the tilt and polarization changes its sign when crossing the wall plane [see Fig. 1(c)]. It is $\Phi_2$ and $P_2$ in the considered $R3c$ phase of BFO. The results of calculations are presented in Figs. 11 and 12. AFD-FE 71° domain walls are almost straight except for the slight bending at the surface (see Fig. 11). The profiles of tilt and polarization components broaden with increase of the tilt gradient coefficient $\nu_{44}$ (compare black, blue, and red curves in Fig. 12). The tilt amplitude remains the same and polarization amplitude decreases with $\nu_{44}$ increase.

Slight bending of the FE domain wall at the surface is determined by an internal electric field that has a nonzero out-of-plane component near the surface (see Fig. S3(b) in the Supplemental Material [52]). The in-plane component of the field is maximal at the domain walls far from the surface (see Fig. S3(a) [52]). The effect is caused by the variation of the in-plane component of polarization $P_1$ perpendicular to the wall due to the coupling with other components of polarization and tilt [see Fig. 11(d)]. However, at the surface the electric field should be perpendicular to it, hence the component $E_1$ tends to zero here (see Fig. S3(a) [52]) and the domain wall–surface junction acts as a source of a stray electric field, causing the wall bending and broadening in this region.

## IV. CONCLUSIONS

Using the LGD approach we reveal zigzaglike meandering AFD-FE domain walls in BFO. These walls typically separate the regions with unusually low monoclinic symmetry. It appeared that the origin of the meandering AFD-FE is conditioned by the decrease of the tilt gradient energy.

Moreover, the origin of the meandering walls does not stem from incomplete polarization screening in thin BFO films, electrostrictive or flexoelectric coupling. The spatial confinement delineates the appropriate boundary conditions for the oxygen tilt and polarization components at the film surfaces, but its existence is not critical for the meandering

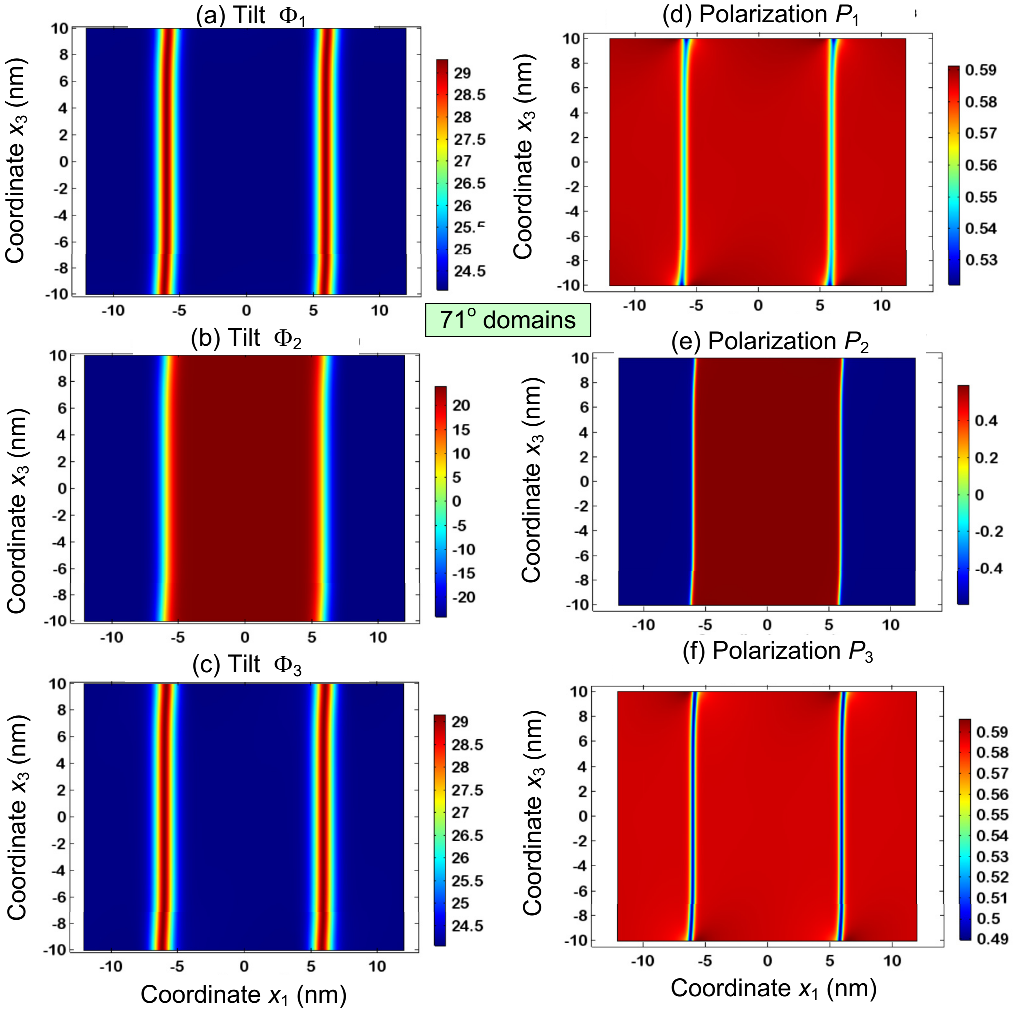

FIG. 11. Distributions of the tilt $\Phi_i$ (a–c) and polarization $P_i$ (d–f) components calculated for the case of 71° domains in a 16-nm BFO film. Gradient coefficient $v_{44} = 0.25 \times 10^{11}\,\mathrm{J/m^3}$; $T = 300\,\mathrm{K}$; BFO parameters are listed in Table I. Initial distribution corresponds to 71° domains with [100] walls.

walls' appearance and their zigzaglike instability. The values of the gradient energy coefficients for the oxygen tilt appeared critical to initiate the morphological changes of the 180° and 109° uncharged domain walls towards zigzag meandering. Zigzag instability appears for small gradient energies, while the walls become straight and broaden at higher gradients. Uncharged 71° walls are always straight and their width increases with increasing of the tilt gradient coefficient.

Hence we identified the gradient-driven morphological phase transition taking place at the AFD-FE domain walls in multiferroics.

## ACKNOWLEDGMENTS

The authors are very grateful to Professor Xiuliang Ma for stimulating discussions and very useful remarks. The work of A.N.M. has received funding from the European Union's Horizon 2020 research and innovation programme under the Marie Skłodowska-Curie Grant Agreement No. 778070, and was partially supported by the National Academy of Sciences of Ukraine (Project No. 0117U002612 and No. 0118U003375) and by the Program of Fundamental Research of the Department of Physics and Astronomy of the National Academy of Sciences of Ukraine (Project No. 0117U000240). The Work is supported (C.T.N., S.V.K.) by the Basic Energy Sciences Division, US Department of Energy.

E.A.E. wrote the codes, performed numerical calculations, and prepared figures. A.N.M. generated the research idea, stated the problem, derived analytical results, and wrote the manuscript draft. E.A.E. and A.N.M. contributed equally to the results interpretation. C.T.N. and S.V.K. worked on the results discussion and manuscript improvement.

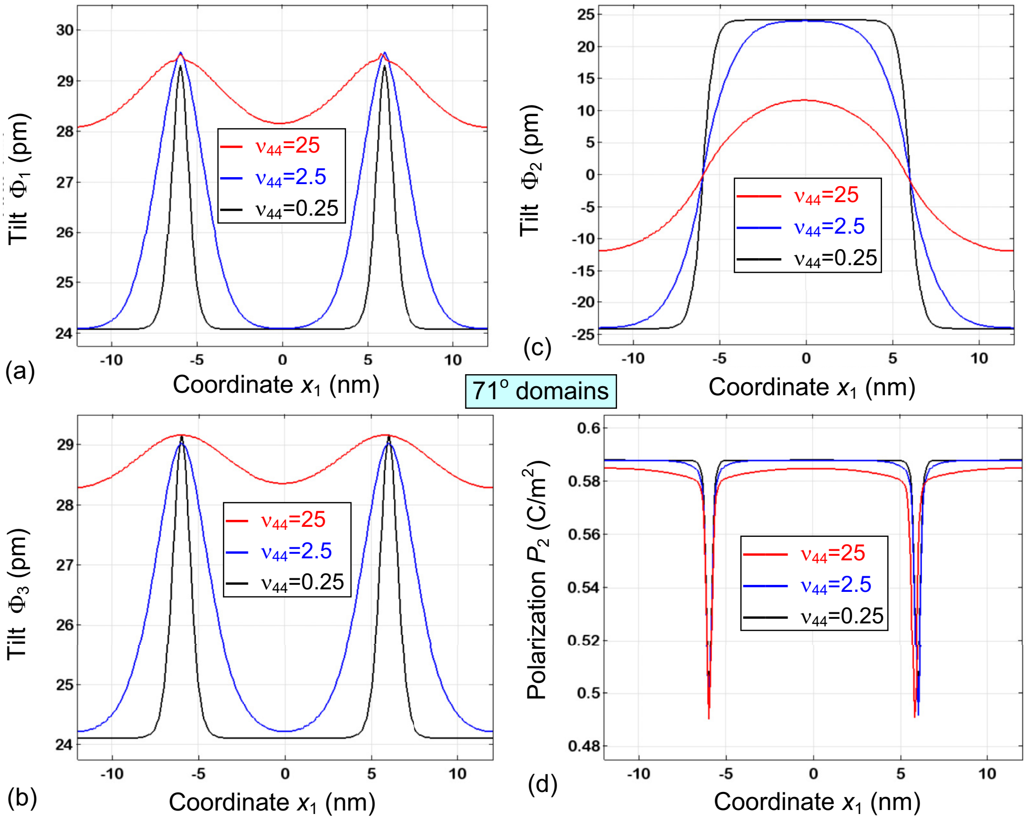

FIG. 12. Profiles of tilts $\Phi_1$ (a), $\Phi_3$ (b), $\Phi_2$ (c), and polarization component $P_3$ (d) at the surface of thin BFO film. The gradient coefficient $\nu_{44} = 0.25 \times 10^{11}$ J/m$^3$ (black curves), $2.5 \times 10^{11}$ J/m$^3$ (blue curves), and $25 \times 10^{11}$ J/m$^3$ (red curves). $T = 300$ K; BFO parameters are listed in Table I.

[1] V. Wadhawan, *Introduction to Ferroic Materials* (CRC Press, Boca Raton, FL, 2000).

[2] H. Jia-Mian, L.-Q. Chen, and C.-W. Nan, Multiferroic heterostructures integrating ferroelectric and magnetic materials, Adv. Mater. **28**, 15 (2016).

[3] A. P. Pyatakov, Magnetoelectricity goes local: From bulk multiferroic crystals to ferroelectricity localized on magnetic topological textures, Phys. B (Amsterdam, Neth.) **542**, 59 (2018).

[4] M. Fiebig, Revival of the magnetoelectric effect, J. Phys. D: Appl. Phys. **38**, R123 (2005).

[5] N. A. Spaldin and M. Fiebig, The renaissance of magnetoelectric multiferroics, Science **309**, 391 (2005).

[6] J. M. Rondinelli and N. A. Spaldin, Structure and properties of functional oxide thin films: Insights from electronic-structure calculations, Adv. Mater. **23**, 3363 (2011).

[7] A. P. Pyatakov and A. K. Zvezdin, Magnetoelectric and multiferroic media, Phys.-Usp. **55**, 557 (2012).

[8] J. F. Scott, Data storage: Multiferroic memories, Nat. Mater. **6**, 256 (2007).

[9] M. Fiebig, T. Lottermoser, D. Meier, and M. Trassin, The evolution of multiferroics, Nat. Rev. Mater. **1**, 16046 (2016).

[10] E. V. Balashova and A. K. Tagantsev, Polarization response of crystals with structural and ferroelectric instabilities, Phys. Rev. B **48**, 9979 (1993).

[11] G. Catalan and J. F. Scott, Physics and applications of bismuth ferrite, Adv. Mater. **21**, 2463 (2009).

[12] V. Gopalan and D. B. Litvin, Rotation-reversal symmetries in crystals and handed structures,Nat. Mater. **10**, 376 (2011).

[13] M. J. Haun, E. Furman, T. R. Halemane, and L. E. Cross, Thermodynamic theory of the lead zirconate-titanate solid solution system, part IV: Tilting of the oxygen octahedra, Ferroelectrics **99**, 55 (1989).

[14] B. Houchmanzadeh, J. Lajzerowicz, and E. Salje, Order parameter coupling and chirality of domain walls, J. Phys.: Condens. Matter **3**, 5163 (1991).

[15] A. K. Tagantsev, E. Courtens, and L. Arzel, Prediction of a low-temperature ferroelectric instability in antiphase domain boundaries of strontium titanate, Phys. Rev. B **64**, 224107 (2001).

[16] A. N. Morozovska, E. A. Eliseev, M. D. Glinchuk, L.-Q. Chen, and V. Gopalan, Interfacial polarization and pyroelectricity in antiferrodistortive structures induced by a flexoelectric effect and rotostriction, Phys. Rev. B **85**, 094107 (2012).

[17] M. Daraktchiev, G. Catalan, and J. F. Scott, Landau theory of domain wall magnetoelectricity, Phys. Rev. B **81**, 224118 (2010).

[18] A. K. Tagantsev, L. E. Cross, and J. Fousek, *Domains in Ferroic Crystals and Thin Films* (Springer, New York, 2010).

[19] A. Y. Borisevich, E. A. Eliseev, A. N. Morozovska, C.-J. Cheng, J.-Y. Lin, Y.-H. Chu, D. Kan, I. Takeuchi, V. Nagarajan, and S. V. Kalinin, Atomic-scale evolution of modulated phases at the ferroelectric–antiferroelectric morphotropic phase boundary

controlled by flexoelectric interaction, Nat. Commun. **3**, 775 (2012).

[20] A. K. Tagantsev, K. Vaideeswaran, S. B. Vakhrushev, A. V. Filimonov, R. G. Burkovsky, A. Shaganov, D. Andronikova, A. I. Rudskoy, A. Q. R. Baron, H. Uchiyama, D. Chernyshov, A. Bosak, Z. Ujma, K. Roleder, A. Majchrowski, J.-H. Ko, and N. Setter, The origin of antiferroelectricity in $PbZrO_3$, Nat. Commun. **4**, 2229 (2013).

[21] P. Henning and E. K. H. Salje, Flexoelectricity, incommensurate phases and the Lifshitz point, J. Phys.: Condens. Matter **28**, 075902 (2016).

[22] R. G. Burkovsky, A. K. Tagantsev, K. Vaideeswaran, N. Setter, S. B. Vakhrushev, A. V. Filimonov, A. Shaganov, D. Andronikova, A. I. Rudskoy, A. Q. R. Baron, and H. Uchiyama, Lattice dynamics and antiferroelectricity in $PbZrO_3$ tested by x-ray and Brillouin light scattering, Phys. Rev. B **90**, 144301 (2014).

[23] E. A. Eliseev, S. V. Kalinin, Y. Gu, M. D. Glinchuk, V. Khist, A. Borisevich, V. Gopalan, L.-Q. Chen, and A. N. Morozovska, Universal emergence of spatially modulated structures induced by flexoantiferrodistortive coupling in multiferroics, Phys. Rev. B **88**, 224105 (2013).

[24] V. Goian, S. Kamba, O. Pacherova, J. Drahokoupil, L. Palatinus, M. Dusek, J. Rohlıcek, M. Savinov, F. Laufek, W. Schranz, A. Fuith, M. Kachlık, K. Maca, A. Shkabko, L. Sagarna, A. Weidenkaff, and A. A. Belik, Antiferrodistortive phase transition in $EuTiO_3$, Phys. Rev. B **86**, 054112 (2012).

[25] J.-W. Kim, P. Thompson, S. Brown, P. S. Normile, J. A. Schlueter, A. Shkabko, A. Weidenkaff, and P. J. Ryan, Emergent Superstructural Dynamic Order Due to Competing Antiferroelectric and Antiferrodistortive Instabilities in Bulk $EuTiO_3$, Phys. Rev. Lett. **110**, 027201 (2013).

[26] R. Maran, S. Yasui, E. A. Eliseev, M. D. Glinchuk, A. N. Morozovska, H. Funakubo, I. Takeuchi, and N. Valanoor, Interface control of a morphotropic phase boundary in epitaxial samarium-modified bismuth ferrite superlattices, Phys. Rev. B **90**, 245131 (2014).

[27] Y. M. Jin, Y. U. Wang, A. G. Khachaturyan, J. F. Li, and D. Viehland, Adaptive ferroelectric states in systems with low domain wall energy: Tetragonal microdomains, J. Appl. Phys. **94**, 3629 (2003).

[28] Y. M. Jin, Y. U. Wang, A. G. Khachaturyan, J. F. Li, and D. Viehland, Conformal Miniaturization of Domains with Low Domain-Wall Energy: Monoclinic Ferroelectric States near the Morphotropic Phase Boundaries, Phys. Rev. Lett. **91**, 197601 (2003).

[29] Y. U. Wang, Three intrinsic relationships of lattice parameters between intermediate monoclinic $M_C$ and tetragonal phases in ferroelectric $Pb[(Mg_{1/3}Nb_{2/3})_{1-x}Ti_x]O_3$ and $Pb[(Zn_{1/3}Nb_{2/3})_{1-x}Ti_x]O_3$ near morphotropic phase boundaries, Phys. Rev. B **73**, 014113 (2006).

[30] S. Kaufmann, U. K. Roßler, O. Heczko, M. Wuttig, J. Buschbeck, L. Schultz, and S. Fahle, Adaptive Modulations of Martensites, Phys. Rev. Lett. **104**, 145702 (2010).

[31] A. N. Morozovska, E. A. Eliseev, S. V. Kalinin, L.-Q. Chen, and V. Gopalan, Surface polar states and pyroelectricity in ferroelastics induced by flexo-roto field, Appl. Phys. Lett. **100**, 142902 (2012).

[32] A. N. Morozovska, E. A. Eliseev, S. L. Bravina, A. Y. Borisevich, and S. V. Kalinin, Roto-flexoelectric coupling impact on the phase diagrams and pyroelectricity of thin $SrTiO_3$ films, J. Appl. Phys. **112**, 064111 (2012).

[33] N. A. Pertsev, A. K. Tagantsev, and N. Setter, Phase transitions and strain-induced ferroelectricity in $SrTiO_3$ epitaxial thin films, Phys. Rev. B **61**, R825 (2000).

[34] A. N. Morozovska, Y. Gu, V. V. Khist, M. D. Glinchuk, L.-Q. Chen, V. Gopalan, and E. A. Eliseev, Low-symmetry monoclinic ferroelectric phase stabilized by oxygen octahedra rotations in strained $Eu_xSr_{1-x}TiO_3$ thin films, Phys. Rev. B **87**, 134102 (2013).

[35] N. A. Pertsev, A. G. Zembilgotov, and A. K. Tagantsev, Effect of Mechanical Boundary Conditions on Phase Diagrams of Epitaxial Ferroelectric Thin Films, Phys. Rev. Lett. **80**, 1988 (1998).

[36] O. Diéguez, S. Tinte, A. Antons, C. Bungaro, J. B. Neaton, K. M. Rabe, and D. Vanderbilt, *Ab initio* study of the phase diagram of epitaxial $BaTiO_3$, Phys. Rev. B **69**, 212101 (2004).

[37] Y. L. Li and L. Q. Chen, Temperature-strain phase diagram for $BaTiO_3$ thin films, Appl. Phys. Lett. **88**, 072905 (2006).

[38] A. Gruverman, D. Wu, H.-J. Fan, I. Vrejoiu, M. Alexe, R. J. Harrison, and J. F. Scott, Vortex ferroelectric domains, J. Phys.: Condens. Matter **20**, 342201 (2008).

[39] A. K. Yadav, C. T. Nelson, S. L. Hsu, Z. Hong, J. D. Clarkson, C. M. Schlepütz, A. R. Damodaran, P. Shafer, E. Arenholz, L. R. Dedon, D. Chen, A. Vishwanath, A. M. Minor, L. Q. Chen, J. F. Scott, L. W. Martin, and R. Ramesh, Observation of polar vortices in oxide superlattices, Nature **530**, 198 (2016).

[40] N. Balke, B. Winchester, W. Ren, Y. H. Chu, A. N. Morozovska, E. A. Eliseev, M. Huijben, R. K. Vasudevan, P. Maksymovych, J. Britson, S. Jesse, I. Kornev, R. Ramesh, L. Bellaiche, L.-Q. Chen, and S. V. Kalinin, Enhanced electric conductivity at ferroelectric vortex cores in $BiFeO_3$, Nat. Phys. **8**, 81 (2012).

[41] B. Winchester, N. Balke, X. X. Cheng, A. N. Morozovska, S. Kalinin, and L. Q. Chen, Electroelastic fields in artificially created vortex cores in epitaxial $BiFeO_3$ thin films, Appl. Phys. Lett. **107**, 052903 (2015).

[42] G. Catalan, H. Béa, S. Fusil, M. Bibes, P. Paruch, A. Barthélémy, and J. F. Scott, Fractal Dimension and Size Scaling of Domains in Thin Films of Multiferroic $BiFeO_3$, Phys. Rev. Lett. **100**, 027602 (2008).

[43] S. V. Kalinin, B. J. Rodriguez, J. D. Budai, S. Jesse, A. N. Morozovska, A. A. Bokov, and Z. G. Ye, Direct evidence of mesoscopic dynamic heterogeneities at the surfaces of ergodic ferroelectric relaxors, Phys. Rev. B **81**, 064107 (2010).

[44] V. V. Shvartsman and A. L. Kholkin, Domain structure of $0.8Pb(Mg_{1/3}Nb_{2/3})O_3$-$0.2PbTiO_3$ studied by piezoresponse force microscopy, Phys. Rev. B **69**, 014102 (2004).

[45] K. S. Wong, J. Y. Dai, X. Y. Zhao, and H. S. Luo, Time-and temperature-dependent domain evolutions in poled (111)-cut $(Pb(Mg_{1/3}Nb_{2/3})O_3)_{0.7}(PbTiO_3)_{0.3}$ single crystal, Appl. Phys. Lett. **90**, 162907 (2007).

[46] A. Kholkin, A. Morozovska, D. Kiselev, I. Bdikin, B. Rodriguez, P. Wu, A. Bokov, Z.-G. Ye, B. Dkhil, L.-Q. Chen, M. Kosec, and S. V. Kalinin, Surface domain structures and mesoscopic phase transition in relaxor ferroelectrics, Adv. Funct. Mater. **21**, 1977 (2011).

[47] A. N. Morozovska, E. A. Eliseev, J. Wang, G. S. Svechnikov, Y. M. Vysochanskii, V. Gopalan, and L.-Q. Chen, Phase diagram and domain splitting in thin ferroelectric films with incommensurate phase, Phys. Rev. B **81**, 195437 (2010).

[48] A. Artemev, B. Geddes, J. Slutsker, and A. Roytburd, Thermodynamic analysis and phase field modeling of domain structures in bilayer ferroelectric thin films, J. Appl. Phys. **103**, 074104 (2008).

[49] A. Hubert and R. Schafer, *Magnetic Domains: The Analysis of Magnetic Microstructures* (Springer, Berlin, 1998).

[50] E. A. Eliseev, Y. M. Fomichov, S. V. Kalinin, Y. M. Vysochanskii, P. Maksymovich, and A. N. Morozovska, Labyrinthine domains in ferroelectric nanoparticles: Manifestation of a gradient-induced morphological phase transition, Phys. Rev. B **98**, 054101 (2018).

[51] A. N. Morozovska, Y. M. Fomichov, P. Maksymovych, Y. M. Vysochanskii, and E. A. Eliseev, Analytical description of domain morphology and phase diagrams of ferroelectric nanoparticles, Acta Mater. **160**, 109 (2018).

[52] See Supplemental Material at http://link.aps.org/supplemental/10.1103/PhysRevB.99.014112 for evident form of the free energy and corresponding equations of state.

[53] D. C. Arnold, K. S. Knight, G. Catalan, S. A. T. Redfern, J. F. Scott, P. Lightfoot, and F. D. Morrison, The $\beta$-to-$\gamma$ transition in $BiFeO_3$: A powder neutron diffraction study, Adv. Funct. Mater. **20**, 2116 (2010).

[54] R. Palai, R. S. Katiyar, H. Schmid, P. Tissot, S. J. Clark, J. Robertson, S. A. T. Redfern, G. A. Catalan, and J. F. Scott, $\beta$ phase and $\gamma-\beta$ metal-insulator transition in multiferroic $BiFeO_3$, Phys. Rev. B **77**, 014110 (2008).

[55] P. Fischer, M. Polomska, I. Sosnowska, and M. Szymanski, Temperature dependence of the crystal and magnetic structures of $BiFeO_3$, J. Phys. C: Solid State Phys. **13**, 1931 (1980).

[56] O. Dieguez, P. Aguado-Puente, J. Junquera, and J. Iniguez, Domain walls in a perovskite oxide with two primary structural order parameters: First-principles study of $BiFeO_3$, Phys. Rev. B **87**, 024102 (2013).

[57] Q. He, C.-H. Yeh, J.-C. Yang, G. Singh-Bhalla, C.-W. Liang, P.-W. Chiu, G. Catalan, L. W. Martin, Y.-H. Chu, J. F. Scott, and R. Ramesh, Magnetotransport at Domain Walls in $BiFeO_3$, Phys. Rev. Lett. **108**, 067203 (2012).

[58] G. Catalan, J. Seidel, R. Ramesh, and J. F. Scott, Domain wall nanoelectronics, Rev. Mod. Phys. **84**, 119 (2012).

[59] A. Y. Borisevich, O. S. Ovchinnikov, H. J. Chang, M. P. Oxley, P. Yu, J. Seidel, E. A. Eliseev, A. N. Morozovska, R. Ramesh, S. J. Pennycook, and S. V. Kalinin, Mapping octahedral tilts and polarization across a domain wall in $BiFeO_3$ from Z-contrast scanning transmission electron microscopy image atomic column shape analysis, ACS Nano **4**, 6071 (2010).

[60] A. N. Morozovska, R. K. Vasudevan, P. Maksymovych, S. V. Kalinin, and E. A. Eliseev, Anisotropic conductivity of uncharged domain walls in $BiFeO_3$, Phys. Rev. B. **86**, 085315 (2012).

[61] R. K. Vasudevan, A. N. Morozovska, E. A. Eliseev, J. Britson, J.-C. Yang, Y.-H. Chu, P. Maksymovych, L. Q. Chen, V. Nagarajan, and S. V. Kalinin, Domain wall geometry controls conduction in ferroelectrics, Nano Lett. **12**, 5524 (2012).

[62] R. K. Vasudevan, W. Wu, J. R. Guest, A. P. Baddorf, A. N. Morozovska, E. A. Eliseev, N. Balke, V. Nagarajan, and P. Maksymovych, Domain wall conduction and polarization-mediated transport in ferroelectrics, Adv. Funct. Mater. **23**, 2592 (2013).

[63] D. V. Karpinsky, E. A. Eliseev, F. Xue, M. V. Silibin, A. Franz, M. D. Glinchuk, I. O. Troyanchuk, S. A. Gavrilov, V. Gopalan, L.-Q. Chen, and A. N. Morozovska, Thermodynamic potential and phase diagram for multiferroic bismuth ferrite ($BiFeO_3$), npj Comput. Mater. **3**, 20 (2017).

[64] J. Wang, J. B. Neaton, H. Zheng, V. Nagarajan, S. B. Ogale, B. Liu, D. Viehland, V. Vaithyanathan, D. G. Schlom, U. V. Waghmare, N. A. Spaldin, K. M. Rabe, M. Wuttig, and R. Ramesh, Epitaxial $BiFeO_3$ multiferroic thin film heterostructures, Science **299**, 1719 (2003).

[65] Y.-H. Chu, Q. Zhan, L. W. Martin, M. P. Cruz, P.-L. Yang, G. W. Pabst, F. Zavaliche, S.-Y. Yang, J.-X. Zhang, L.-Q. Chen, D. G. Schlom, I.-N. Lin, T.-B. Wu, and R. Ramesh, Nanoscale domain control in multiferroic $BiFeO_3$ thin films, Adv. Mater. **18**, 2307 (2006).

[66] Y.-H. Chu, L. W. Martin, M. B. Holcomb, M. Gajek, S.-J. Han, Q. He, N. Balke, C.-H. Yang, D. Lee, W. Hu, Q. Zhan, P.-L. Yang, A. Fraile-Rodríguez, A. Scholl, S. X. Wang, and R. Ramesh, Electric-field control of local ferromagnetism using a magnetoelectric multiferroic, Nat. Mater. **7**, 478 (2008).

[67] P. Maksymovych, M. Huijben, M. Pan, S. Jesse, N. Balke, Y.-H. Chu, H. J. Chang, A. Y. Borisevich, A. P. Baddorf, G. Rijnders, D. H. A. Blank, R. Ramesh, and S. V. Kalinin, Ultrathin limit and dead-layer effects in local polarization switching of $BiFeO_3$, Phys. Rev. B **85**, 014119 (2012).

[68] C. Beekman, W. Siemons, M. Chi, N. Balke, J. Y. Howe, T. Z. Ward, P. Maksymovych, J. D. Budai, J. Z. Tischler, R. Xu, W. Liu, and H. M. Christen, Ferroelectric self-poling, switching, and monoclinic domain configuration in $BiFeO_3$ thin films, Adv. Funct. Mater. **26**, 5166 (2016).

[69] M. Trassin, G. De Luca, S. Manz, and M. Fiebig, Probing ferroelectric domain engineering in $BiFeO_3$ thin films by second harmonic generation, Adv. Mater. **27**, 4871 (2015).

[70] W. Y. Wang, Y. L. Tang, Y. L. Zhu, Y. B. Xu, Y. Liu, Y. J. Wang, S. Jagadeesh, and X. L. Ma, Atomic level 1D structural modulations at the negatively charged domain walls in $BiFeO_3$ films, Adv. Mater. Interfaces **2**, 1500024 (2015).

[71] W. Y. Wang, Y. L. Zhu, Y. L. Tang, Y. B. Xu, Y. Liu, S. Li, S. R. Zhang, Y. J. Wang, and X. L. Ma, Large scale arrays of four-state vortex domains in $BiFeO_3$ thin film, Appl. Phys. Lett. **109**, 202904 (2016).

[72] J. Nordlander, G. De Luca, N. Strkalj, M. Fiebig, and M. Trassin, Probing ferroic states in oxide thin films using optical second harmonic generation, Appl. Sci. **8**, 570 (2018).

[73] W. Y. Wang, Y. L. Zhu, Y. L. Tang, M. J. Han, Y. J. Wang, and X. L. Ma, Atomic mapping of structural distortions in 109 degrees domain patterned $BiFeO_3$ thin films, J. Mater. Res. **32**, 2423 (2017).

[74] M. J. Han, Y. J. Wang, D. S. Ma, Y. L. Zhu, Y. L. Tang, Y. Liu, N. B. Zhang, J. Y. Ma, and X. L. Ma, Coexistence of rhombohedral and orthorhombic phases in ultrathin $BiFeO_3$ films driven by interfacial oxygen octahedral coupling, Acta Mater. **145**, 220 (2018).

[75] E. A. Eliseev, M. D. Glinchuk, V. Gopalan, and A. N. Morozovska, Rotomagnetic couplings influence on the magnetic properties of antiferrodistortive antiferromagnets, J. Appl. Phys. **118**, 144101 (2015).

[76] A. N. Morozovska, E. A. Eliseev, M. D. Glinchuk, O. M. Fesenko, V. V. Shvartsman, V. Gopalan, M. V. Silibin, and D. V. Karpinsky, Rotomagnetic coupling in fine-grained multiferroic $BiFeO_3$: Theory and experiment, Phys. Rev. B **97**, 134115 (2018).

[77] J. H. Barrett, Dielectric constant in perovskite type crystals, Phys. Rev. **86**, 118 (1952).

[78] Y. Gu, K. Rabe, E. Bousquet, V. Gopalan, and L.-Q. Chen, Phenomenological thermodynamic potential for $\mathrm{CaTiO_3}$ single crystals, Phys. Rev. B **85**, 064117 (2012).

[79] A. K. Tagantsev and G. Gerra, Interface-induced phenomena in polarization response of ferroelectric thin films, J. Appl. Phys. **100**, 051607 (2006).

[80] J. Bardeen, Surface states and rectification at a metal semiconductor contact, Phys. Rev. **71**, 717 (1947).

[81] M. J. Highland, T. T. Fister, D. D. Fong, P. H. Fuoss, C. Thompson, J. A. Eastman, S. K. Streiffer, and G. B. Stephenson, Equilibrium Polarization of Ultrathin $\mathrm{PbTiO_3}$ with Surface Compensation Controlled by Oxygen Partial Pressure, Phys. Rev. Lett. **107**, 187602 (2011).

[82] G. B. Stephenson and M. J. Highland, Equilibrium and stability of polarization in ultrathin ferroelectric films with ionic surface compensation, Phys. Rev. B **84**, 064107 (2011).

[83] S. V. Kalinin, Y. Kim, D. Fong, and A. Morozovska, Surface-screening mechanisms in ferroelectric thin films and their effect on polarization dynamics and domain structures, Rep. Prog. Phys. **81**, 036502 (2018).

[84] A. N. Morozovska, E. A. Eliseev, I. S. Vorotiahin, M. V. Silibin, S. V. Kalinin, and N. V. Morozovsky, Control of polarization hysteresis temperature behavior by surface screening in thin ferroelectric films, Acta Mater. **160**, 57 (2018).

[85] E. A. Eliseev, A. V. Semchenko, Y. M. Fomichov, M. D. Glinchuk, V. V. Sidsky, V. V. Kolos, Y. M. Pleskachevsky, M. V. Silibin, N. V. Morozovsky, and A. N. Morozovska, Surface and finite size effects impact on the phase diagrams, polar and dielectric properties of $\mathrm{(Sr, Bi)Ta_2O_9}$ ferroelectric nanoparticles, J. Appl. Phys. **119**, 204104 (2016).

[86] E. A. Eliseev, I. S. Vorotiahin, Y. M. Fomichov, M. D. Glinchuk, S. V. Kalinin, Y. A. Genenko, and A. N. Morozovska, Defect driven flexo-chemical coupling in thin ferroelectric films, Phys. Rev. B **97**, 024102 (2018).

[87] A. K. Tagantsev, G. Gerra, and N. Setter, Short-range and long-range contributions to the size effect in metal-ferroelectric-metal heterostructures, Phys. Rev. B **77**, 174111 (2008).

[88] J. Wang, A. K. Tagantsev, and N. Setter, Size effect in ferroelectrics: Competition between geometrical and crystalline symmetries, Phys. Rev. B **83**, 014104 (2011).

[89] Actually, the boundary condition $D_3|_{x_3=h+0} - D_3|_{x_3=h-0} = \sigma(\varphi) \equiv -\frac{\varepsilon_0\varphi}{\Lambda}|_{x_3=h}$ can be transformed to the equivalent condition, $(D_3|_{x_3=h+0} - D_3|_{x_3=h-0})\Lambda = -\varepsilon_0\varphi|_{x_3=h}$. Therefore, the limit $\Lambda \rightarrow 0$ in the boundary condition $(D_3|_{x_3=h+0} - D_3|_{x_3=h-0})\Lambda = -\varepsilon_0\varphi|_{x_3=h}$ simply means that $\varphi|_{x_3=h} \rightarrow 0$ at $\Lambda \rightarrow 0$, which is equivalent to zero potential $(\varphi|_{x_3=h} = 0)$ at film contact with conducting electrode, and the screening takes place in the electrode. On the other hand, the screening length is zero in an ideal conductor, and in this sense one can consider that “the screening charges take infinitesimal space at $\Lambda = 0$.

[90] L. D. Landau and E. M. Lifshitz, *Theory of Elasticity. Theoretical Physics* (Butterworth-Heinemann, Oxford, 1976), Vol. 7.

[91] D. R. Tilley, Finite-size effects on phase transitions in ferroelectrics, *Ferroelectic Thin Films*, edited by C. Paz de Araujo, J. F. Scott, and G. W. Teylor (Gordon and Breach, Amsterdam, 1996), pp. 11–45.

[92] I. Dzyaloshinsky, A thermodynamic theory of “weak” ferromagnetism of antiferromagnetics, J. Phys. Chem. Solids **4**, 241 (1958).

[93] S. V. Kalinin, A. N. Morozovska, L. Q. Chen, and B. J. Rodriguez, Local polarization dynamics in ferroelectric materials, Rep. Prog. Phys. **73**, 056502 (2010).

[94] Since we used the variational method for the solution of equations of state, the stability of the solution is guaranteed by the calculation algorithm itself, and the numerical algorithm converges to the local energy minimum. However, we cannot guarantee that the numerical algorithm can find the absolute minimum in the general case. Therefore the solutions with approximately equal negative energies can be classified as long-living metastable states.

[95] D. Vanderbilt and M. H. Cohen, Monoclinic and triclinic phases in higher-order Devonshire theory, Phys. Rev. B **63**, 094108 (2001).

[96] S. Conti, S. Muller, A. Poliakovsky, and E. K. H. Salje, Coupling of order parameters, chirality, and interfacial structures in multiferroic materials, J. Phys.: Condens. Matter **23**, 142203 (2011).